FINAL PERFORMANCE REPORT
(F49620-02-1-0243)

Executive Summary

To improve the high-cycle fatigue (HCF) behavior of critical components of gas turbine engines, a thin layer of subsurface compressive residual stress is often imparted on the components with some surface enhancement technique, which may also induce changes in subsurface texture and microstructure. The objectives of this project were: (I) to develop an ultrasound technique for nondestructive inspection of the residual stress layer in aluminum and titanium induced by the surface treatment of low plasticity burnishing (LPB), and (II) to determine the preferred subsurface stress and texture conditions for optimal fatigue performance.

Under objective (I), a method was developed to estimate the surface residual stress and texture of an LPB-treated, flat metal surface by simultaneous measurement of Rayleigh waves and surface skimming longitudinal waves. The method showed promise in the successful recovery of surface residual stress in an AA 7076-T651 aluminum sample surface-treated by low plasticity burnishing.

Under objective (II), the effects of sandblasting and shot peening on a commercially pure titanium (Ti), a Ti-6Al-4V alloy, and two Al-Cu alloys (AA 2026 and 2099) were investigated, and a theoretical analysis of the effects of micro-texture on the behavior of short fatigue crack growth was undertaken. The main findings of this part of the project are as follows:

- Short fatigue cracks were initiated in the α-phase grains of the Ti-6Al-4V alloy studied. They propagated crystallographically within the α-phase grains, and non-crystallographically in the β-phase grains. The fatigue life of the Ti-6Al-4V alloy was prolonged by shot peening or re-peening both at room temperature and at 150 °C.

- Commercially pure titanium specimens, which were sandblasted, exhibited higher HCF strength than the untreated titanium specimens. Annealing subsequent to sandblasting generated a nano-crystalline surface layer, which resulted in better corrosion performance of the specimens than sandblasting alone.

- After the surface enhancement treatments of shot peening and sandblasting, hardening textures were formed in the treated surface layer: a B-texture was formed in the Ti-6Al-4V alloy after shot peening and in pure titanium after sandblasting.

- The enhancement of fatigue properties by surface enhancement treatments was not only due to the formation of beneficial surface residual stress, but was also due to strain hardening, texture strengthening and grain refinement in the alloys studied.

- A method based on the macro-texture in an alloy was developed to evaluate the resistance to fatigue crack growth in the alloy.

- By studying the effects of micro- and macro-texture on fatigue properties in AA 2026 and 2099 Al alloys, it was found that, given the measured global texture and grain structure in these alloys, the resistance to crack growth could be quantified by calculating all the possible twist angles of crack deflection at grain boundaries,. This calculated resistance qualitatively correlated well with the observed crack growth behavior of these alloys.

20060601091

REPORT DOCUMENTATION PAGE

AFRL-SR-AR-TR-06-0116

The public reporting burden for this collection of information is estimated to average 1 hour per response, including the 1 gathering and maintaining the data needed, and completing and reviewing the collection of information. Send comments rega information, including suggestions for reducing the burden, to the Department of Defense, Executive Services and Commur that notwithstanding any other provision of law, no person shall be subject to any penalty for failing to comply with a colle control number.

PLEASE DO NOT RETURN YOUR FORM TO THE ABOVE ORGANIZATION.

1. REPORT DATE *(DD-MM-YYYY)* 05/10/2006	2. REPORT TYPE Final Performance Report	3. DATES COVERED *(From - To)* 06/01/2002 - 10/31/2005

4. TITLE AND SUBTITLE	5a. CONTRACT NUMBER
Residual Stress, Micro-and Macrotexture in Surface-Enhanced Titanium Alloys: Their Nondestructive Inspection and Effects on High-Cycle Fatigue Properties	F49620-02-1-0243

5b. GRANT NUMBER

5c. PROGRAM ELEMENT NUMBER

6. AUTHOR(S)	5d. PROJECT NUMBER
Chi-Sing Man, Tongguang Zhai	

5e. TASK NUMBER

5f. WORK UNIT NUMBER

7. PERFORMING ORGANIZATION NAME(S) AND ADDRESS(ES) University of Kentucky Research Foundation 201 Kinkead Hall Lexington, KY 40506-0057	8. PERFORMING ORGANIZATION REPORT NUMBER

9. SPONSORING/MONITORING AGENCY NAME(S) AND ADDRESS(ES) USAF, AFRL Air Force Office of Scientific Research 875 North Randolph Street Arlington, VA 22203 Dr Arje Nachman	10. SPONSOR/MONITOR'S ACRONYM(S) AFOSR/NM
	11. SPONSOR/MONITOR'S REPORT NUMBER(S)

12. DISTRIBUTION/AVAILABILITY STATEMENT

Approved for public release; distribution is unlimited. — Distribution A

13. SUPPLEMENTARY NOTES

14. ABSTRACT

An acoustoelastic method was developed to estimate the residual stress and texture of a flat metal surface by simultaneous measurement of Rayleigh waves and surface skimming longitudinal waves (or P waves). The method showed promise in the successful recovery of surface residual stress in an AA 7076-T651 aluminum sample surface-treated by low plasticity burnishing. The effects of sandblasting and shot peening on a commercially pure titanium, a Ti-6Al-4V titanium alloy, and two Al-Cu aluminum alloys (AA 2026 and 2099) were investigated, and a theoretical analysis of the effects of micro-texture on the behavior of short fatigue crack growth was undertaken.

15. SUBJECT TERMS

acoustoelasticity, residual stress, low plasticity burnishing, nondestructive evaluation, Rayleigh waves, P waves, laser-ultrasonics, high cycle fatigue, texture, micro-texture, sandblasting, shot peening, re-peening, fatigue crack growth, aluminum, titanium

16. SECURITY CLASSIFICATION OF:			17. LIMITATION OF ABSTRACT	18. NUMBER OF PAGES	19a. NAME OF RESPONSIBLE PERSON
a. REPORT	b. ABSTRACT	c. THIS PAGE		48	19b. TELEPHONE NUMBER *(Include area code)*

Standard Form 298 (Rev. 8/98)
Prescribed by ANSI Std. Z39.18

Personnel Associated with this Project

- Principal investigator: Chi-Sing Man.
- Co-principal investigator: Tongguang Zhai.
- Postdoctoral associate: Wenchang Liu.
- Graduate students: Zhiqiang Cai, Xiuping Jiang, Jinxia Li, Leigh L. Noble, Yu Xiang.
- Undergraduate student: James T. Zellers.
- Others: Jin Li, visiting scholar; Xingyan Fan, laboratory technician.

Publications Resulting from this Project

<u>Journal Papers</u>

1. K. Tanuma, C.-S. Man, M. Huang, and G. Nakamura, "Surface impedance tensors of textured polycrystals", *Journal of Elasticity* **67**, 131–147 (2002).

2. K. Tanuma and C.-S. Man, "Angular dependence of Rayleigh-wave velocity in prestressed polycrystalline media with monoclinic texture", *Journal of Elasticity* **69** (2002), 181–214 (2003).

3. M. Huang and C.-S. Man, "Constitutive relation of elastic polycrystal with quadratic texture dependence", *Journal of Elasticity* **72**, 183–212 (2003).

4. S. A. Ivanov, C.-S. Man, and G. Nakamura, "Recovery of residual stress in a vertically heterogeneous medium", *IMA Journal of Applied Mathematics* **70**, 129–146 (2005).

5. M. Huang and C.-S. Man, "A finite-element study on constitutive relation HM-V for elastic polycrystals", *Computational Materials Science* **32**, 378–386 (2005).

6. T. Zhai, X.P. Jiang, J.X. Li, M.D. Garratt, G.H. Bray, "The grain boundary geometry for optimum resistance to growth of short fatigue cracks in high strength Al-alloys", *International Journal of Fatigue* **27**, 1202–1209 (2005).

7. J.X. Li, T. Zhai, M.D. Garratt, G.H. Bray, "Four point bend fatigue of AA2026 Al alloys", *Metallurgical and Materials Transactions A* **36**, 2529–2539 (2005).

8. C.-S. Man, R. Paroni, Y. Xiang, and E.A. Kenik, "On the geometric autocorrelation function of polycrystalline materials", *Journal of Computational and Applied Mathematics* **190**, 200–210 (2006).

9. T. Zhai, "Strength distribution of fatigue crack initiation sites in an Al-Li alloy", *Metallurgical and Materials Transactions A*, accepted.

10. X.P. Jiang, X.Y Huang, J.X. Li, D.Y. Li, C.-S. Man, M.J. Shepard, and T. Zhai, "Enhancement of fatigue and corrosion properties of pure Ti by sandblasting", *Materials Science and Engineering A*, accepted.

11. K. Tanuma and C.-S. Man, "Perturbation formula for phase velocity of Rayleigh waves in prestressed anisotropic media", *Journal of Elasticity*, accepted.

Papers in Conference Proceedings

1. G. Nakamura, C.-S. Man, and K. Tanuma, "Dispersion formula of the Rayleigh wave", invited paper in *Proceedings of the Second International Conference on Structural Stability and Dynamics (Singapore, 16-18 December 2002)*, C.M. Wang et al. (eds.), World Scientific, Singapore, 2002, pp. 152–158.

2. K. Tanuma, C.-S. Man, M. Huang, and G. Nakamura, "Surface impedance tensors of textured polycrystals", in *Proceedings of the Second International Conference on Structural Stability and Dynamics (Singapore, 16-18 December 2002)*, C.M. Wang et al. (eds.), World Scientific, Singapore, 2002, pp. 768–773.

3. T. Zhai, A. Wilkinson, and J.W. Martin, "Orientation dependence of high cycle fatigue properties in a hot-cross rolled Al-Li 8090 alloy plate", in *Aluminum Alloys 2002 (Proc. of ICAA8)*, *Materials Science Forum*, Vols. 396-402, 2002, pp. 1279–1284.

4. T. Zhai, "A mechanism for fatigue crack initiation in pure metal", in *Materials Lifetime Science and Engineering*, P.K. Liaw et al. (eds.), TMS (The Minerals, Metals and Materials Society), Warrendale, PA, 2003, pp. 91–98.

5. L .L. Noble, C.-S. Man, and G. Nakamura, "Recovery of through-thickness texture profile in sheet metals by resonance spectroscopy", in *Review of Progress in Quantitative Nondestructive Evaluation (Green Bay, Wisconsin July 27–August 1, 2003)*, vol. 23, D.O. Thompson and D.E. Chimenti (eds.), American Institute of Physics, Melville, New York, 2004, pp. 1232–1239.

6. Z. Cai, C.-S. Man, and X. Fan, "Resonance-EMAT measurements on aluminum sheets with monoclinic texture", submitted to *Review of Progress in Quantitative Nondestructive Evaluation (Green Bay, Wisconsin July 27–August 1, 2003)*, vol. 24, D.O. Thompson and D.E. Chimenti (eds.), American Institute of Physics, Melville, New York.

7. A. Moreau and C.-S. Man, "Laser-ultrasonic measurements of residual stresses on aluminum 7075 surface-treated with low plasticity burnishing", in *Proc. of Materials Science & Technology 2005 Conf.*, Pittsburgh, 25–28 September 2005, pp. 97–108.

8. A. Moreau and C.-S. Man, "Laser-ultrasonic measurements of residual stresses in a 7075-T651 aluminum sample surface-treated with low plasticity burnishing", in *Review of Progress in Quantitative Nondestructive Evaluation*, Vol. 25, D.O. Thompson and D.E. Chimenti (eds.), American Institute of Physics, Melville, New York, 2006, pp. 1434–1441.

Dissertations and Theses

1. L.L. Noble, Recovery of through-thickness texture profiles in orthorhombic sheets of cubic metals by resonance spectroscopy. Doctoral dissertation, University of Kentucky, Lexington, 2004.

2. Y. Xiang, Effects of grain shape and crystallographic texture on plastic anisotrophy of aluminum alloy sheets. Doctoral dissertation, University of Kentucky, Lexington, 2004.

3. Z. Cai, Resonance-EMAT measurements on aluminum sheets with monoclinic texture. M.S. thesis, University of Kentucky, Lexington, 2004.

Final Performance Report

This report is divided into two parts. Part I pertains to work the objective of which is to develop an ultrasound technique for nondestructive inspection of the residual stress layer in titanium induced by the surface treatment of low plasticity burnishing. Part II reports the findings of our investigations on the effects of surface enhancement treatments including sandblasting and shot peening on the microstructure, texture and fatigue properties of a commercially pure titanium, a Ti-6Al-4V alloy, and two Al-Cu alloys (AA 2026 and 2099). Part I of the report below was written by Chi-Sing Man, and Part II by Tongguang Zhai.

PART I

Introduction

Low plasticity burnishing (LPB) is an emerging surface-enhancement technique [1], by which a thin subsurface layer of compressive residual stress is imparted on metal parts to improve their high-cycle fatigue behavior and material damage tolerance. To incorporate the beneficial effect of such surface treatment into component-life predictions, some inspection method has to be developed so that the profile of the subsurface stress layer can be measured or inferred nondestructively, both before and after the treated part is put into service. At present, for titanium and aluminum alloys, no nondestructive measurement technique is available for this purpose.

The presence of a subsurface layer of inhomogeneous residual stress in an otherwise homogeneous medium should lead to the dispersion of Rayleigh waves, which raises the possibility that we could infer some information on the profile of the residual stress from this acoustoelastic effect. Preliminary studies by Man et al. [2, 3] suggested that this acoustoelastic approach should merit further investigation. The first part of the present project is a follow-up of those preliminary studies. While our ultimate aim is for applications to titanium, we and our research partners at the Air Force Research Laboratory (AFRL) decided to focus our work first on an AA 7075-T651 aluminum alloy to study the feasibility of this acoustoelastic approach.

Method

The approach adopted in our project was based on four considerations:

A. The residual stress induced by LPB treatment results from plastic deformations, and the displacements involved in the propagation of the superimposed ultrasonic waves are small. Hence a natural theoretical setting for the present study is linear elasticity with initial stress [4, 5]. This theory is applicable so long as the superimposed infinitesimal motion could be taken as elastic; whether the prestress comes from plastic deformations such as those incurred during LPB treatment has no bearing on the validity of the theory.

B. Polycrystalline metal samples usually acquire crystallographic texture through the manufacturing processes that produce them, and low plasticity burnishing itself typically

leads to changes in the surface and subsurface texture of the metal part treated. Therefore using a constitutive relation which accounts explicitly for the effects of crystallographic texture is crucial. Such a constitutive relation can be obtained for cubic and for hexagonal metals by extending the earlier work of Man et al. [6–8].

C. Since low plasticity burnishing leaves a mirror-smooth surface finish, surface roughness has no place in our theoretical treatment. In our work, we restricted our attention to the effects of residual stress and crystallographic texture on the dispersion of Rayleigh waves propagating along a flat surface.

D. In acoustoelastic measurement of stress, the effects of stress must be separated from those of texture. In our project an attempt to effect this separation was made by using laser ultrasonics to make simultaneous measurements of two acoustic modes, namely Rayleigh waves and surface-skimming longitudinal waves (or P waves). This would not have been possible should we work with conventional ultrasonics. In conventional ultrasonics, using multiple acoustic modes requires multiple transducers, and it is necessary in measurements to use a contact or bonding material between the transducer and the sample. This will make it virtually impossible, whenever multiple transducers are used, to achieve the measurement accuracy required by the smallness of the acoustoelastic effect, because it is extremely difficult to make bonds with sufficiently reproducible ultrasonic qualities. Laser-ultrasonics is a technology whereby ultrasound is generated and detected optically with lasers. In laser-ultrasonics, all acoustic modes are generated at once and the problem of contact is avoided altogether.

Theoretical Findings

In our project we explored using Rayleigh waves and surface skimming longitudinal (or P) waves in combination for nondestructive inspection of the layer of compressive residual stress imparted on metal parts by the surface enhancement technique of low plasticity burnishing (LPB). The surface stress and subsurface stress profile are to be inferred from measurement of Rayleigh-wave and surface skimming P-wave velocities as functions of propagation direction and frequency. So far, our theoretical work on Rayleigh waves propagating along the free surface of a vertically inhomogeneous, prestressed half-space is largely completed, but further work remains to be done to elucidate the nature of the P pulse. Here is an outline of what we did.

Consider a vertically inhomogeneous, prestressed elastic half space $x_3 \leq 0$ in the Cartesian coordinate space (x_1, x_2, x_3) with the free surface $x_3 = 0$. The displacement $u = (u_1, u_2, u_3)$ satisfies the equation of motion

$$\rho \frac{\partial^2 u_i}{\partial t^2} = \sum_{j,k,l=1}^{3} \frac{\partial}{\partial x_j} \left(\left(T_{jl}^0 \delta_{ik} + L_{ijkl} \right) \frac{\partial u_k}{\partial x_l} \right) \quad \text{in } x_3 < 0, \quad i = 1,2,3 \quad (1)$$

and the zero-traction boundary condition on $x_3 = 0$. Here $\rho > 0$ is the mass density, t the time, T^0 the residual stress, and L the incremental elasticity tensor, which depends on T^0 and the

5

orientation distribution function w that describes crystallographic texture. We assume that T^o and L are functions of x_3 only.

For Rayleigh waves, our purpose is to derive a high-frequency asymptotic formula for the phase velocity or, more precisely, to develop a procedure for expressing each term of the asymptotic expansion of the velocity for large wave number k in terms of T^o and L and their higher-order x_3-derivatives at $x_3 = 0$. Our procedure consists of the following four steps:

1. For large wave numbers k, construct an asymptotic solution of the equation of motion and the traction-free boundary condition in the form

$$u = U\left(n_1, n_2, x_3, v, k\right) \exp\left(-\sqrt{-1}\, k\left(n_1 x_1 + n_2 x_2 - vt\right)\right),$$

where v is the phase velocity, $n = (n_1, n_2, 0)$ is the direction of propagation, and U is a complex vector function which decays exponentially as $x_3 \rightarrow -\infty$.

2. Compute the corresponding surface traction t at $x_3 = 0$.

3. Find 3×3 surface impedance matrix Z in the asymptotic form

$$Z = k Z_0(v, n) + Z_1(v, n) + k^{-1} Z_2(v, n) + k^{-2} Z_3(v, n) + \dots$$

for large k, which transforms linearly displacement u to surface traction t at $x_3 = 0$.

4. Apply the implicit function theorem to $\det Z(k, v, n) = 0$ to obtain an asymptotic formula for the phase velocity v for large k:

$$v = v(k, n) = v_0(n) + k^{-1} v_1(n) + k^{-2} v_2(n) + \dots .$$

For simplicity of notation, in the formulae above we have suppressed the dependence of Z_m and v_m on T^o and L and their higher-order x_3-derivatives at $x_3 = 0$. In fact, Z_0 and v_0 are functions of T^o and L at $x_3 = 0$; for $m \geq 1$ and $1 \leq l \leq m$, Z_m and v_m are functions of T^o and L and their x_3-derivatives of l-th order at $x_3 = 0$. In earlier work we have obtained [9] an explicit formula for v_0 for monoclinic media, which is later generalized to the case of arbitrary anisotropy [10]; these formulae are useful for recovery of surface stress. Now we have derived an explicit procedure for the computation of Z_m and v_m. This procedure will play a crucial role when we consider the inverse problem of determining the depth profile of residual stress from the observed dispersion of Rayleigh-wave velocity.
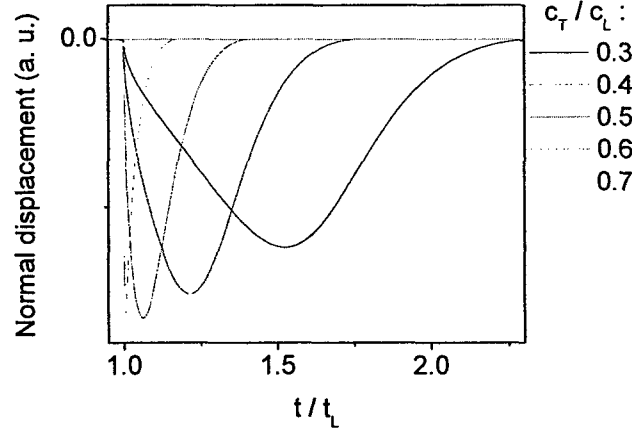
Figure 1. Simulated pulse shape of the P wave for different ratios of c_T/c_L for a homogeneous isotropic medium (Bescond et al., [15]).

At present there is [11–14] still no consensus among researchers on the physical nature of the surface skimming longitudinal wave (or P wave) nor on its dispersion. Figure 1 shows in numerical simulations (Bescond et al., [15]) how the shape of the P pulse varies with the ratio of shear and longitudinal wave velocities for the surface response to an impulsive line source acting on the surface of a homogeneous isotropic half-space. The leading edge of the P pulse seems to propagate with the velocity of the longitudinal wave, but the shape of the pulse depends on the velocity ratio. With the caveat that further work remains to be done to elucidate the nature of the P pulse, in what follows, in our attempt to recover the surface residual stress we simply assume that the leading edge of the P pulse satisfies the same velocity formula as that of bulk longitudinal waves propagating in a medium with the elastic properties of the free surface.

A Feasibility Study

To explore the feasibility of our present acoustoelastic approach, an attempt was made [16, 17] to recover the surface residual stress imparted by low plasticity burnishing on an AA 7075-T651 aluminum sample. In this study, a simplified model for the acoustoelastic response of weakly-textured aggregates of cubic metals was used to describe the dependence of ultrasound on texture and residual stress. The details of the mathematical model are presented elsewhere [16]. In summary, we assume that the material is a polycrystalline aggregate of cubic material with overall orthorhombic symmetry and a weak texture. Let the normal direction to the free surface be the 3-axis, and the reference (rolling) direction in the plane of the surface be the 1-axis. Then, the model predictions of the Rayleigh wave velocity, V_R, and of the P wave velocity, V_P, are

$$\frac{V_R - V_{R0}}{V_{R0}} = \alpha_R W_{400} + \beta_R W_{420} \cos 2(\theta - \theta_W) + \gamma_R W_{440} \cos 4(\theta - \theta_W) + \delta_R T_m + \varepsilon_R T_d \cos 2(\theta - \theta_{RS}), \quad (2)$$

$$\frac{V_P - V_{P0}}{V_{P0}} = \alpha_P W_{400} + \beta_P W_{420} \cos 2(\theta - \theta_W) + \gamma_P W_{440} \cos 4(\theta - \theta_W) + \delta_P T_m + \varepsilon_P T_d \cos 2(\theta - \theta_{RS}), \quad (3)$$

where the subscripts $R0$ and $P0$ refer to the velocities in a material with isotropic texture and no residual stresses, θ is the angle between the propagation direction and the 1-axis, θ_W is the angle between the reference direction of texture and the 1-axis, σ_a and σ_b are the principal stresses in the (principal) a- and b-direction, respectively, θ_{RS} is the angle between the a-direction and the 1-axis, $T_m = (\sigma_b + \sigma_a)/2$, $T_d = (\sigma_b - \sigma_a)/2$. The W_{4m0} coefficients are the fourth-order crystallographic orientation distribution coefficients. The Greek letter symbols depend on single crystal elastic properties. They can either be obtained from micromechanical models or from calibration experiments. In our work on the AA 7075-T651 sample, we used the HM-V$_c$ model [18] and the Man-Paroni model [7, 19] to compute the values of these parameters from the single-crystal second-order [20] and third-order elastic constants [21] of aluminum. Equations (2) and (3) are used to calculate the relative change of the Rayleigh wave velocities, $\Delta V_R/V_{R0}$ and $\Delta V_P/V_{P0}$, respectively, caused by surface processing. After algebraic manipulations, one finds that

$$\Delta V_R / V_{R0} = (V''_R - V'_R)/V_{R0} = A_R + B_R \cos 2\theta + C_R \sin 2\theta + D_R \cos 4\theta + E_R \sin 4\theta, \quad (4)$$

where the parameters A_R through E_R are combinations of the material parameters α_R to ε_R, the W_{4m0}, T_m and T_d, θ_W and θ_{RS}, and where the prime and double prime refer to the material before and after LPB processing, respectively. Similarly, another equation is obtained for $\Delta V_P/V_{P0}$ where the subscripts R are replaced by P, namely:

$$\Delta V_P / V_{P0} = (V''_P - V'_P)/V_{P0} = A_P + B_P \cos 2\theta + C_P \sin 2\theta + D_P \cos 4\theta + E_P \sin 4\theta. \quad (5)$$

Equations (4) and (5) can be fitted to the data using a simple multiple linear least squares fit. The expressions for the fitted parameters A to E are inverted to obtain the following information about changes in residual stresses and texture:

$$\Delta T_m = T''_m - T'_m = \frac{\alpha_P A_R - \alpha_R A_P}{\alpha_P \delta_R - \alpha_R \delta_P} \quad \text{and} \quad \Delta W_{400} = W''_{400} - W'_{400} = \frac{\delta_P A_R - \delta_R A_P}{\alpha_R \delta_P - \alpha_P \delta_R} \quad (6)$$

(see [16] for more details and for equations on the other texture coefficients and θ_W); and if it can be assumed that $T'_d = 0$, then

$$\theta''_{RS} = \frac{1}{2} \arctan\left(\frac{\beta_R C_P - \beta_P C_R}{\beta_R B_P - \beta_P B_R}\right), \quad (7)$$

$$T''_d = \frac{\beta_R B_P - \beta_P B_R}{(\beta_R \varepsilon_P - \beta_P \varepsilon_R)\cos 2\theta''_{RS}} = \frac{\beta_R C_P - \beta_P C_R}{(\beta_R \varepsilon_P - \beta_P \varepsilon_R)\sin 2\theta''_{RS}}. \quad (8)$$

These equations are completely decoupled from texture modification that could arise at the surface from the LPB process. Note that only the 2θ dependence of the ultrasound velocity is required to characterize the residual stress anisotropy. However, the B and C parameters cannot be evaluated simultaneously without evaluating A and at least one of D, E, or some combination

of D and E. Therefore, measurements at four different angles are necessary and sufficient to evaluate T''_m, T''_d, and θ''_{RS} if the material surface in question has no residual stress prior to processing. One such set of four measurements would be in the directions of $\theta = 0$, $\pi/4$, $\pi/2$, and $3\pi/4$.

To provide a testing ground for the ultrasonic method designed, a subcontract was made to the Industrial Materials Institute (contact: Dr. André Moreau), National Research Council of Canada, for laser-ultrasonic measurements of Rayleigh and P waves on an AA 7076-T651 sample. The sample was a 4"×4"×0.875" block with one half of one of the two square faces LPB-treated. A schematics of the measurement geometry is shown in Fig. 2. A typical ultrasonic signal displaying the time of arrival of the P pulse (near 0.6 µs) and Rayleigh pulse (near 1.2 µs) is shown in Fig. 3. The P-wave frequency content extended from 2 to about 15 MHz, while the Rayleigh-wave frequency content extended from 2 to more that 60 MHz. The relative changes in Rayleigh-wave velocity and P-wave velocity as a functions of frequency and propagation angle are shown in Fig. 4 and Fig. 5, respectively.
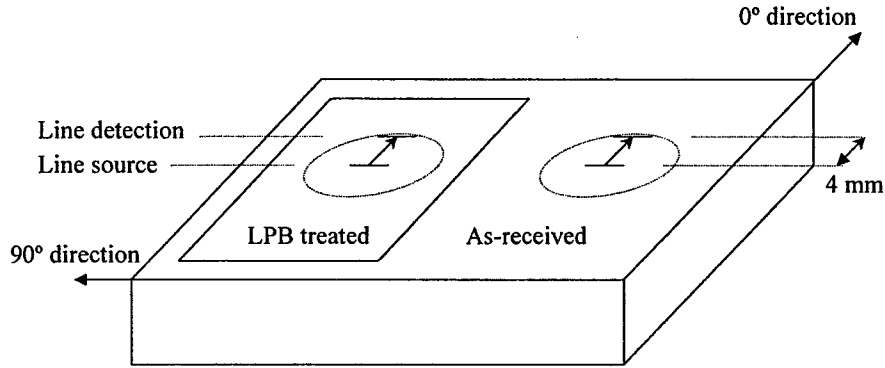
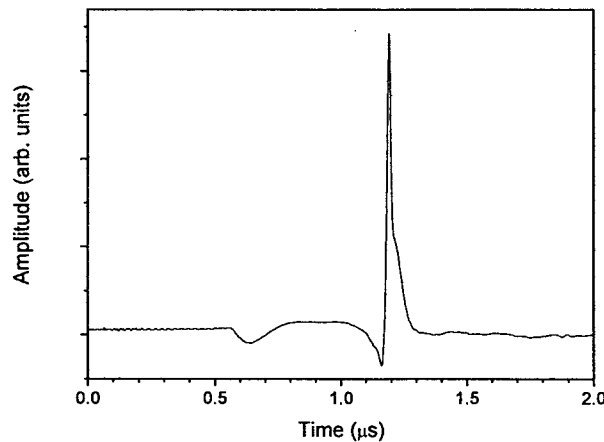Figure 2. Schematics of the measurement setup.

Figure 3. Ultrasonic signal amplitude as a function of time. The P pulse arrives near 0.6 µs. The Rayleigh pulse arrives near 1.2 µs.
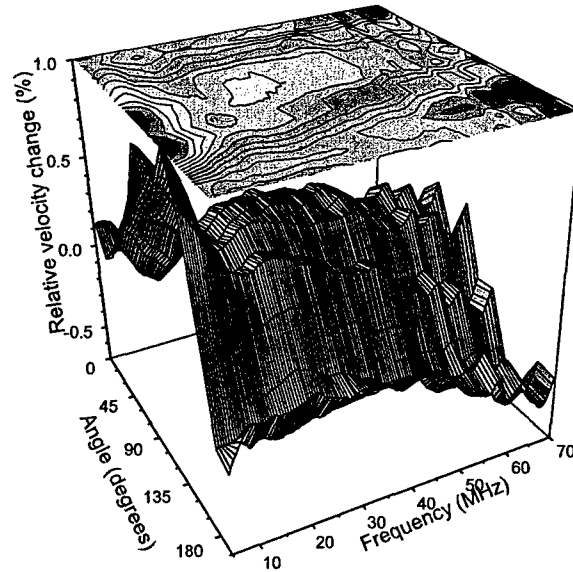
9

Figure 4. Relative change in Rayleigh-wave velocity as a function of frequency and propagation angle. Each contour line represents a relative change of 0.1%.
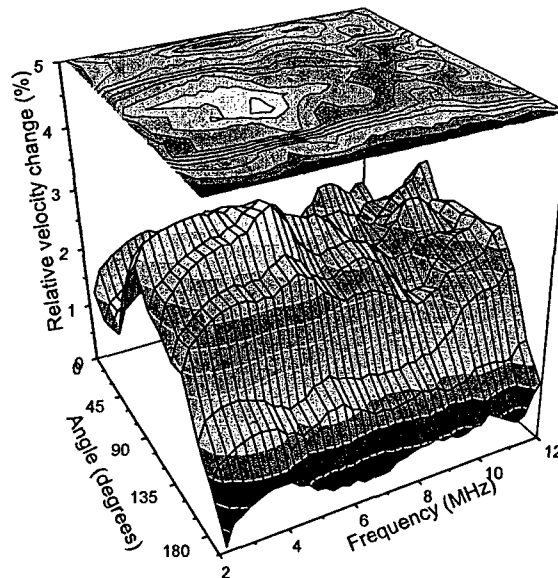

Figure 5. Relative change in P-wave velocity as a function of frequency and propagation direction. Each contour line represents a relative change of 0.294%.
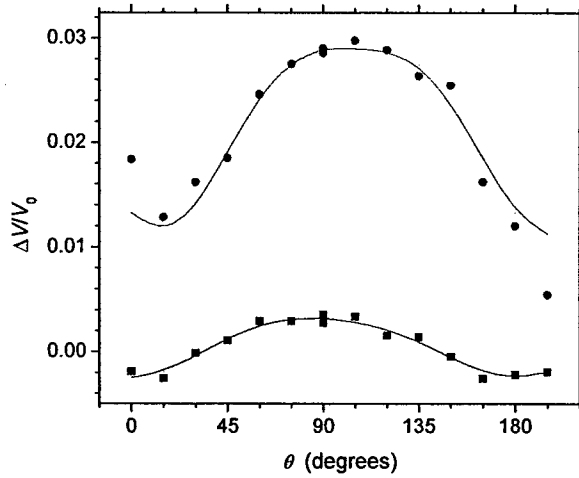
10

Figure 6. Blue square symbols and line: Angular variation of $\Delta V_R / V_{R0}$ in the frequency bandwidth of 20 to 60 MHz. Red circular symbols and line: Angular variation of $\Delta V_P / V_{P0}$ in the frequency bandwidth of 3 to 12 MHz. The symbols are the experimental data and the lines pertain to the fitted model.

Restricting our objective to the measurement of the residual stresses at the surface, the frequency dependence will be neglected. The relative velocity change $\Delta V / V_0$ is averaged in the 20-60 MHz frequency bandwidth for the Rayleigh waves and in the 3-12 MHz frequency bandwidth for the P waves. These are plotted in Fig. 6 and least-squares fitted to Eqs. (4) and (5). The measurement errors are smaller for the Rayleigh waves because these waves are measured with a better signal-to-noise ratio. However, the velocity variations of the P wave are larger. Fig. 6 shows that Rayleigh and P wave velocities have extrema at different angles.

The fitted values (from Fig. 6) of parameters A through E are displayed in Table 1. These values are substituted into Eqs. (6)–(8) to estimate T''_m, T''_d, and θ''_{RS}; here we have assumed that the aluminum sample has no surface stress prior to LPB-treatment. The ultrasonically measured mean residual stress induced by the LPB process is compressive and equal to $T''_m = -498$ MPa. X-ray measurements of the surface residual stresses gave $T''_m = -305$ MPa. Although the agreement may seem poor at first, this is an excellent result. Referring to Eq. (6), we see that T''_m is highly sensitive to errors in A_P, a value that was relatively inaccurate in our measurements

Table 1. Parameters of Eqs. (4) and (5) fitted to the experimental results of Fig. 6. The statistical errors are approximately ± 0.02 % for Rayleigh waves, and ± 0.1 % for P waves.

	A	B	C	D	E
Rayleigh wave	0.075 %	−0.286 %	0.015 %	−0.039 %	−0.008 %
P wave	2.2 %	−0.78 %	−0.42 %	−0.11 %	−0.17 %

because of the large uncertainties involved in correction [17] applied to the measurement method for the effect of surface processing on the generated acoustic P pulse (the correction for the Rayleigh pulse was much more accurate). However, it is quite possible that future development in laser ultrasonic technology will provide a much more accurate value of A_P because the source of inaccuracy is now well understood. The result is also excellent because measurement involving Rayleigh waves only have notoriously failed in the past. Most likely they have failed because they did not take into account texture changes near the surface. In contrast, our measurements account for the effects of texture.

The ultrasonic values of $\theta''_{RS} = 12.4°$ and $T''_d = -143$ MPa indicate that the residual stresses are anisotropic, that the principal axis of σ_a is 12° from the LPB rolling direction, which is also the plate rolling direction. The measured X-ray value $(\sigma_2 - \sigma_1)/2 = -118$ MPa is in general not equal to $T''_d = (\sigma_b - \sigma_a)/2$ because σ_2 and σ_1 are in the LPB-rolling and transverse direction whereas the ultrasonic measurements indicate that σ_b and σ_a are 12° away from those directions. However, we calculate from the ultrasonic data that $(\sigma_2 - \sigma_1)/2 = \frac{1}{2}(\sigma_b - \sigma_a)\cos 2\theta''_{RS} = -130$ MPa. This agrees with the X-ray value to within 10%. Hole drilling measurements obtained by P. Bouchard and A. Moreau [22] of CNRC-IMI gave $T''_m \sim -470$ MPa, $|T''_d|$ decreasing from 110 to 10 MPa, and $\theta''_{RS} \sim 10°$ in the first 500 μm below the surface.

Concluding Remarks

In this project a method was developed to estimate the surface residual stress and texture of an LPB-treated, flat metal surface by simultaneous measurement of Rayleigh waves and surface skimming longitudinal waves. The method showed promise in the successful recovery of surface residual stress in a 7076-T651 aluminum sample surface-treated by low plasticity burnishing. If this method is corroborated in further measurements, then we have developed a technique which

1) provides a measurement of surface residual stress that is decoupled from texture changes caused by the LPB processing used to impart residual stresses;

2) can measure the anisotropy of surface residual stresses, i.e. it can measure. the two principal stresses and their orientation;

3) can provide information on residual stress anisotropy without requiring a reference sample or surface;

4) does not require the *a priori* knowledge of the symmetry directions of surface texture because these are measured;

5) provides a simultaneous measurement of texture and texture changes caused by the process used to impart residual stress. This opens the possibility to obtain a method and technique capable of simultaneously measuring residual stress and cold work (cold work is important for residual stress retention).

Measurement of surface residual stress, however, is only a first step and is not enough. For life-prediction purposes, the profile of stress within a layer of about 1 mm thick beneath the surface is required. To this end, the nature and the dispersion of P waves must be elucidated first. Only after we have acquired this understanding can we attempt at solving the inverse problem of recovering the residual stress profile, because we do need the information from both the Rayleigh and P wave modes to isolate the effects of stress from those due to texture.

References

[1] Information and publications on low plasticity burnishing are available at the web site of Lambda Technologies, http://www.lambdatechs.com/.

[2] C.-S. Man, J. Li, W.-Y. Lu, and X. Fan, "Ultrasonic measurement of through-thickness stress gradients in textured sheet metals", in *Review of Progress in Quantitative Nondestructive Evaluation*, Vol. 19, D.O. Thompson and D.E. Chimenti (eds.), American Institute of Physics, Melville, New York, 2000, pp. 1613–1620.

[3] C.-S. Man, L. Koo, and M.J. Shepard, "Dispersion of Rayleigh waves in titanium alloy resulting from inhogeneous residual stress induced by low plasticity burnishing", in *Review of Progress in Quantitative Nondestructive Evaluation*, Vol. 21, D.O. Thompson and D.E. Chimenti (eds.), American Institute of Physics, Melville, New York, 2002, pp. 1651–1658.

[4] A. Hoger, "On the determination of residual stress in an elastic body", *J. Elasticity* **16**, 303–324 (1986).

[5] C.-S. Man and W.Y. Lu, "Towards an acoustoelastic theory for measurement of residual stress", *J. Elasticity* **17**, 159–182 (1987).

[6] C.-S. Man, "On the constitutive equations of some weakly-textured materials", *Arch. Rational Mech. Anal.* **143**, 77–103 (1998).

[7] R. Paroni and C.-S. Man, "Constitutive equations of elastic polycrystalline materials", *Arch. Rational Mech. Anal.* **150**, 153–177 (1999).

[8] C.-S. Man, "Effects of crystallographic texture on the acoustoelastic coefficients of polycrystals", *Nondestructive Testing and Evaluation* **15**, 191–214 (1999).

[9] G. Nakamura, C.-S. Man, and K. Tanuma, "Dispersion formula of the Rayleigh wave", invited paper in *Proceedings of the Second International Conference on Structural Stability and Dynamics (Singapore, 16-18 December 2002)*, C.M. Wang et al. (eds.), World Scientific, Singapore, 2002, pp. 152–158.

[10] K. Tanuma and C.-S. Man, "Angular dependence of Rayleigh-wave velocity in prestressed polycrystalline media with monoclinic texture", *J. Elasticity* **69** (2002), 181–214 (2003).

[11] K.J. Langenberg, P. Fellenger, R. Marklein, "On the nature of the so-called subsurface longitudinal wave and/or the surface longitudinal 'creeping' wave", *Res. Nondest. Eval.* **2**, 59–81 (1990).

[12] C.T. Schröder and W.R. Scott, "On the complex conjugate roots of the Rayleigh equation: The leaky surface wave", *J. Acoust. Soc. Am.* **110**, 2867–2877 (2001).

[13] J.G. Harris and J.D. Achenbach, "Comment on 'On the complex conjugate roots of the Rayleigh equation: The leaky surface wave'", *J. Acoust. Soc. Am.* **112**, 1747–1748 (2002).

[14] V.N. Danilov, "Calculations of parameters of longitudinal surface waves on a free planar boundary of a material", *Russian J. Nondestr. Testing* **37**, 700–707 (2001).

[15] C. Bescond et al., "Determination of residual stresses using laser-generated surface skimming longitudinal waves" in *Proc. SPIE Vol. 5767, Nondestr. Eval. and Health Monitoring of Aerospace Mat., Composites, and Civil Infrastructure IV*, P. J. Shull, A. L. Gyekenyesi and A. A. Mufti (eds.), SPIE, The Internat. Soc. for Opt. Eng., 2005, pp. 175–186.

[16] A. Moreau and C.-S. Man, "Laser-ultrasonic measurements of residual stresses on aluminum 7075 surface-treated with low plasticity burnishing", in *Proc. of Materials Science & Technology 2005 Conf.*, Pittsburgh, 25–28 September 2005, pp. 97–108.

[17] A. Moreau and C.-S. Man, "Laser-ultrasonic measurements of residual stresses in a 7075-T651 aluminum sample surface-treated with low plasticity burnishing", in *Review of Progress in Quantitative Nondestructive Evaluation*, Vol. 25, D.O. Thompson and D.E. Chimenti (eds.), American Institute of Physics, Melville, New York, 2006, pp. 1434–1441.

[18] M. Huang and C.-S. Man, "Constitutive relation of elastic polycrystal with quadratic texture dependence", *Journal of Elasticity* **72**, 183–212 (2003).

[19] C.-S. Man and R. Paroni, "On the separation of stress-induced and texture-induced birefringence in acoustoelasticity", *Journal of Elasticity* **45**, 91–116 (1996).

[20] J.F. Thomas, "Third order elastic constants of aluminum", *Phys. Rev.* **175**, 955–962.

[21] V. Sarma and P. Reddy, "Third order elastic constants of aluminum", *Phys. Stat. Sol. A* **10**, 563–567 (1972).

[22] P. Bouchard and A. Moreau, private communications.

14

PART II

1. Introduction

Titanium alloys have been used in many applications including aerospace and aircraft industry because of their high specific strength, good ductility, and perfect fatigue properties. Engine components are subjected to high cycle fatigue (HCF) loading induced by high frequency vibrations within the engine. Since high cycle fatigue is mainly controlled by crack initiation and propagation, to find a method to retard the process of fatigue crack initiation and growth is an effective way to improve the fatigue resistance of materials. It has been demonstrated that surface enhancement treatments such as shot peening, laser shock peening and low plasticity burnishing, etc. [1-4], are the effective techniques commonly used to improve the HCF properties by inducing a beneficial compressive residual stress in the subsurface of metallic components. Although extensive work has been conducted to study these techniques, the effects of the profile of the induced stress and the possible changes in microstructure and crystalline texture due to the surface treatments have not been well understood on the HCF behaviors of Ti alloys. Microstructure and crystalline texture are among the key factors that control the process of fatigue crack initiation and early growth [5, 6].

This part of the research project was proposed to study the effects of micro- and macro-texture and subsurface compressive stress on HDF properties of Ti alloys. The original specific goals were

- Effects of micro- texture on fatigue behavior,
- Effects of macro-texture in the modified surface layer,
- Effects of the induced residual stress and its profile,
- Modeling of short fatigue crack growth.

During the course of this project, the Ti-6Al-4V alloy used by the Air Force Research Lab (AFRL) could only be provided in a very limited quantity. And this alloy was processed exclusively for AFRL and could hardly be replicated in terms of its microstructure and properties by another producer or laboratory because its microstructure and properties are extremely sensitive to its thermomechanical processing history. As an alternative, we used some new generation high strength Al alloys, such as AA 2026 and 2099, to study the micro- and macro-texture effects on fatigue properties in our study. The results from the study of these alloys will also be of great value to the Air Force, since many other high strength alloys currently used by the Air Force, such as Al-Cu alloys and Ni-based superalloys, etc., are also planar slip alloys and their fatigue properties are very sensitive to micro- and macro-texture [6].

In this project, we studied

- Effects of shot peening-fatigue-re-peening on the HCF behavior of a Ti-6Al-4V alloy,
- Texture and microstructure after shot peening, low plasticity burnishing and sand blasting,
- HCF properties and microstructure of sand blasted Ti,
- Effects of micro- and macro-texture on fatigue properties in AA 2026 Al-Cu alloys,

- Theoretical analysis of the effects of micro-texture on the behavior of short fatigue crack growth.

2. Experiment details

2.1 Experiment materials

Ti–6Al–4V alloy

The chemical composition of Ti–6Al–4V alloy is given in Table 1. The original bar-stock (63.5 mm in diameter) was sectioned into segments 400 mm long, preheated to 940 °C for 30 min and forged into 400×150×20 mm plates. These plates were solution heat treated at 925 °C for 1 h, fan air cooled and stabilized at 700°C for 2 h. The microstructure of this alloy was examined in the as-received, bimodal condition, consisting of colonies of equiaxed primary- α and lamellar α + β.

Table 1 Chemical composition of Ti-6Al-4V alloys (wt.%)

		Ti		Al		V		Fe		O		N		H
Ti-6Al-		Bal		6.27		4.19		0.200		0.181		0.012		0.0041

The material used in sandblasting was 35A commercially pure titanium with a thickness of 0.8 mm. The as-received material was annealed at 700°C for 5 minutes. The yield strength of the pure titanium sheet was 360 MPa.
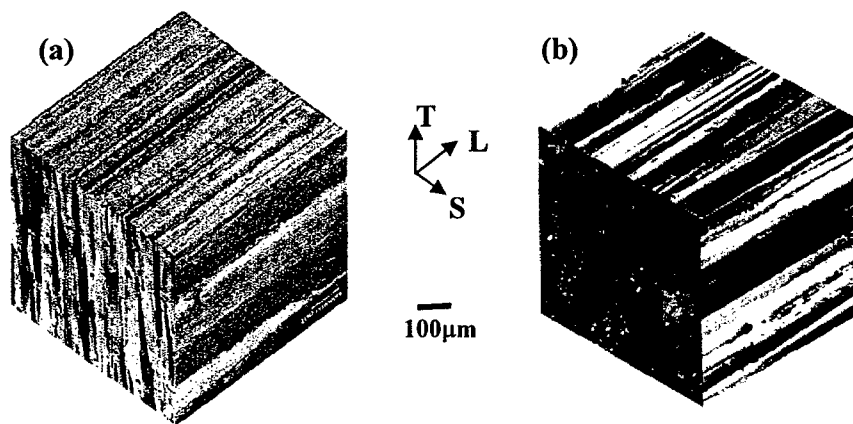
Fig. 1. Optical micrographs of grain structures of a) rectangular and b) square extrusion bars of AA 2026 Al alloys.

The AA 2026 aluminum alloys, newly developed by Alcoa, were in the form of extrusion bars in two different cross-sections, square (120 × 120 mm^2) and rectangular (30 × 470 mm^2). Both of them were in a T351 temper condition which included solution heat-treatment, water quench, 1-3% stretch and natural aging. The chemical composition of the AA 2026 is shown in Table 2. The tensile yield strengths of the square and rectangular bars were 427 MPa and 372 MPa respectively, compared to 290 MPa for their predecessor, AA 2024 Al alloy, in the same temper. These alloys also show superior fatigue limits, above 90% of their yield strengths [7], and fatigue crack growth resistance [8] to those (fatigue limit is about 45% yield strength) of the AA 2024 alloy. They all possess unrecrystallized grain structures — layered and fiber grains in rectangular and square extrusion samples respectively, after hot extrusion and annealing. These alloys could be used as the model materials for studying the effects of micro- and macro-texture on the fatigue behaviors because of their unique grain structures and textures.

Table 2 Chemical composition of the AA 2026 and AA 2024 Al alloy (wt %)

	Si	Fe	Cu	Mn	Mg	Zn	Ti	Zr
AA2026	0.03	0.038	3.95	0.59	1.32	0.013	0.013	0.11
AA2024	0.5	0.5	4.3	0.5	1.5	0.25	-	-

2.2 Experimental Details and theoretical calculation

2.2.1 Fatigue tests

Two types of fatigue tests were conducted in tension-tension and four-point bend in this work. The tension and tension fatigue tests on the 0.8 mm thick pure titanium were carried out in an Instron 8802 servo-hydraulic machine at room temperature. Tensile tests were first performed to obtain the yield strength (σ_y) of the materials. Fatigue tests were then conducted at the maximum stress ranging from $0.4\sigma_y$ to $1.1\sigma_y$, at R=0.1, room temperature and 20 Hz, in air. Fatigue specimens were machined in the same geometry and directions as the tensile specimens, which were prepared according to ASTM standard E8 with 25.4 mm gage length and 6.35 mm gage width.

The geometry of the four-point bend fatigue test samples is shown in Fig. 1b, which led to a uniform stress distribution in the sample surface that was under tension in four-point bend. For AA 2026 Al alloy, high cycle fatigue tests were conducted in the extrusion direction (L) on the L-T and L-S planes of the extrusion bars (Fig. 1a). L, T and S represent the extrusion longitudinal, long transverse and short transverse directions respectively. Sample surfaces were ground using SiC water proof grinding papers ranging from 220 grit to 1200 grit, and polished using first a Al_2O_3 powder of 1 mm in size and then a silica colloidal liquid.
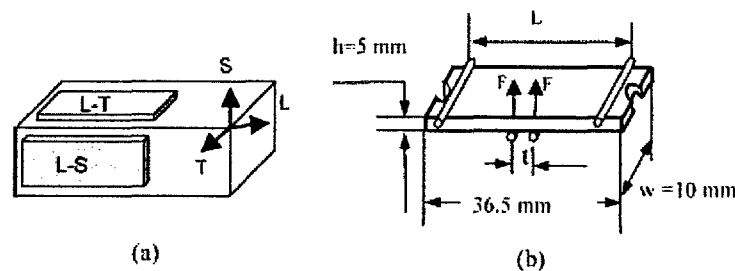
Fig. 1 Schematic diagrams showing the samples for four-point bend fatigue (a) the orientation and location of the samples taken from the extrusion bars (AA 2026 Al alloy) and (b) sample dimensions and testing geometry.

In both these two tests, the maximum cyclic stresses for all alloys were normalized by their yield strength. The fatigue tests were conducted at a stress ratio (R) of 0.1, a sinusoidal waveform, 20 Hz and room temperature, in air. The maximum stress ranged from $0.4\sigma_y$ to $1.1\sigma_y$. The specimens were cycled with constant stress amplitude until failure, or for 5×10^6 cycles if they do not fail.

2.2.2 Microstructure and short crack observation

Optical microscopy was used to observe the microstructures of the alloys and short crack initiation and propagation. Scanning electron microscopy (SEM) was used to investigate the features of the samples surfaces and the fatigue fracture surfaces, and EDS was for the chemical composition analysis of the alloys.

2.2.3 Surface Enhancement Treatments

Shot peening is routinely used treat the surface of critical engine components subject to high cycle fatigue failure. Because high velocity metal/ceramic beads blast against the surface of the components randomly, a highly cold worked surface layer and a compressive surface residual stress are produced. Ti-6Al-4V specimens with two different dimensions were used in this study, 40 mm x 15 mm x 5 mm (for four point bend fatigue tests) and 25.4 mm x 25.4 mm x 4 mm (for texture measurement). They were shot peened to an intensity of 6A using MI-170-R cast steel shot with 125% coverage. The shot peening treatment was arranged by our partner in AFRL, . After being fatigued at 150 °C and a constant maximum stress of 75% σ_y for half of their life expectancy, the shot peened samples were re-peened using the same peening procedure to study the residual stress relaxation effect on the fatigue behavior.

Low plasticity burnishing (LPB) on some of the Ti-6Al-4V samples was also conducted by Lambda Research, Inc. Since Lambda Research, Inc. could only process those Ti-6Al-4V samples that were used for texture measurement by XRD and ultrasound, the effects of low plasticity burnishing was not studied on the HCF properties of the alloy. However, some researchers from Lambda Research, Inc. have recently published the results indicating LPB has a beneficial effect on the HCF properties of the alloy [4, 9, 10].

18

Sandblasting is primarily used for surface cleaning and rust removing of engineering materials. However, if used properly, e.g., by adjusting the incident angle of high speed SiO_2 particles and blasting coverage, of repeatedly impacted the surface of the titanium sheet, which resulted in a severely deformed surface layer which is under a compressive residual stress. The material used in the present investigation was 35A commercially pure titanium with a thickness of 1 mm. The as-received material was annealed to recrystallize at 700 °C for 5 minutes. It was subsequently sandblasted with SiO_2 particles of 200-300 μm in diameter. The pressure of the compressed air used for sandblasting was about 300 psi. The magnitude of the compressive stress induced by sandblasting was typically controlled by varying air pressure, the angle of blasting, and the size and shape of the particles. The surface roughness, Ra, of the sandblasted sample was measured by a Taylor-Hobson Form Talysurf-50 machine.

2.2.4 Orientations determination

The textures of pure titanium, Ti-6Al-4V and AA 2026 were measured by an X-ray diffraction method. (0002), $(10\bar{1}0)$, $(10\bar{1}1)$, and $(10\bar{1}2)$ pole figures for Ti and $\{111\}$, $\{200\}$, $\{220\}$ and $\{311\}$ pole figures for AA 2026 were measured up to a maximum tilt angle of 75° using Schulz back reflection method. The orientation distribution functions (ODFs) were calculated from these four measured incomplete pole figures and presented as plots of constant φ_2 sections with isointensity contours in Euler space defined by the Euler angles φ_1, Φ, and φ_2.

Electron back scatter diffraction (EBSD) was used to determine the orientations of the grains that interacted with cracks, in order to relate the behavior of fatigue crack growth with micro- and macro-texture. For the EBSD experiments, the sample surfaces were either etched or electropolished, in the final step of sample preparation, to obtain decent Kikuchi patterns for orientation analysis.

2.2.5 Twist and tilt angle calculation

Zhai, et al. have previously studied the geometry of short fatigue crack deflection across grain boundaries in Al-Li alloys in details with an electron back scatter diffraction (EBSD) technique [6]. The twist component of crack deflection has been found to be the key factor controlling crack growth across these grain boundaries in the Al-Li alloys. As illustrated in Fig. 2 which shows a model for crack deflection at a grain boundary, the twist angle, α, has to be minimized for the crack to propagate through the boundary, since the triangle area, **abc**, covered by α on the boundary plane has to be fractured. The fracture of **abc** presents a significant barrier to crack growth across the boundary. The larger the twist angle, the higher the resistance to crack growth will be. A large α can thus lead to significant retardation or even arrest of short cracks. Note that the tilt angle, β, and Schmidt factor of a slip plane can also affect crack growth across a grain boundary to certain degree, since they both can affect the driving force of crack growth. α and β can be determined by measuring the orientation of grains 1 and 2 and matching to the crack path on the surface, using the following equations,

$$\alpha = \arccos([E]\times[N_1]\bullet[E]\times[N_2])$$
$$\beta = \arccos([Z]\times[N_1]\bullet[Z]\times[N_2])$$

(1)

19

where [E] and [Z] are unit vectors of grain boundary plane and sample surface normals, and [N_1] and [N_2] are unit vectors of normals of the two favored slip planes in the neighboring grains. [N_1] and [N_2] can be measured by EBSD. [E] and [Z] may be known from grain structure and sample geometry.
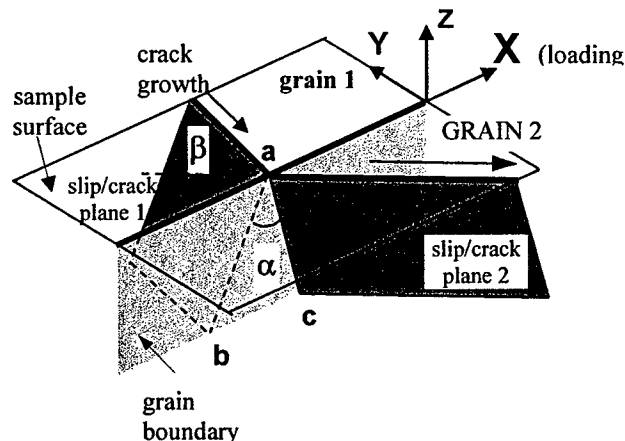

Fig. 2 Schematic diagram showing a crystallographic mechanism for crack growth along slip plane 1 in grain 1 onto slip plane 2 in grain 2.

3. Experimental results

3.1 As-Received and shot peened Ti-6Al-4V

3.1.1 Fatigue properties of Ti-6Al-4V

Four-point bend fatigue tests were carried out respectively on the as-received and shot peened Ti-6Al-4V at room temperature and 150 °C. The fatigue strength of these samples was then measured. In order to save the testing material, a step test method which used a single specimen to determine the endurance limit was used to measure the fatigue limits of these samples [11]. Shot peening improved the fatigue limit of the Ti-6Al-4V alloy, as shown in Table 3. Generally, the surface residual stress generated by shot peening will be relaxed at an elevated temperature, which may cancel out the beneficial effect of the residual stress on the fatigue property by of the components. In this study, however, the fatigue limit of Ti-6Al-4V measured at 150 °C was even slightly higher than that measured at room temperature. In fact, the fatigue limits of the shot peened Ti-6Al-4V samples fatigued at room temperature and 150 °C were almost same, indicating that the fatigue properties might not be affected by this temperature.

When the shot peened specimens were tested under cyclic loading at 150 °C, the compressive residual stresses were relaxed via thermo-mechanical mechanisms. However, mechanical relaxation might be the dominated mechanism in this case, since 150 °C was so lower that residual stress might not be relaxed or slightly relaxed. Kodama [12] measured residual stress decrease of the surface of shot peened specimens by XRD. He reported that the compressive residual stress in the first load cycle could be relaxed by more than 50%. At the numbers of

cycles N > 1, the residual stress relaxation could be calculated by the following linear logarithm relation [12],

$$\sigma_N^{re} = A + m \lg N \qquad (2)$$

where σ_N^{re} is the surface residual stress after N cycles, A and m are material constants depending on the stress amplitude.

Researchers found that at a slightly elevated temperature (150 °C), fatigue crack growth rates of a near-alpha alloy were lower than that at room temperature [13]. It may also be possible that it was partially caused by the test error often associated with high cycle fatigue tests, as only one sample was used in this measurement. More works should be done to clearly understand the effect of temperature on fatigue properties in shot peened Ti-6Al-4V alloy.

Table 3 Fatigue limits of Ti-6Al-4V in different conditions

As-received (room)	Shot peened Ti-6Al-4V (room)	Shot peened Ti-6Al-4V (150°C)
65% σ_y	71% σ_y	72%σ_y

The compressive residual stress induced by shot peening could not only delay crack initiation, but also slow down crack propagation. Fig. 3 is the residual stress profile of the shot peened Ti-6Al-4V. The compressive residual stresses were confined to a shallow surface layer, within 200 μm deep. The compressive residual stress reached the maximum value of 800 MPa at about 25 μm below the surface.
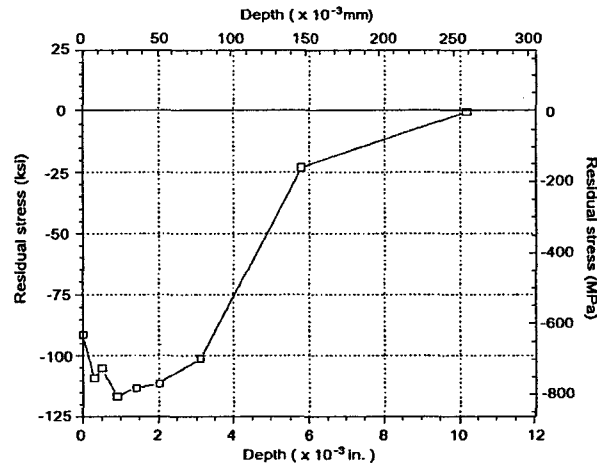
Fig. 3 The profile of residual stress of shot peened Ti-6Al-4V

Re-shot-peening is a common practice in the maintenance operation of airplane structures, which could prolong the service life of expensive components, such as gas turbine engine components. Similarly, in this research, the fatigue limits of shot peened Ti-6Al-4V at room temperature and 150 °C were obtained using the step test method, as listed in Table 3. Once the fatigue limits were determined, the fatigue lives of the shot peened Ti-6Al-4V alloy at a higher stress level (the maximum stress was 75% σ_y) at room temperature and 150 °C were measured. Then, three other specimens were fatigued for half of the fatigue life at the same stress level (the maximum stress

was 75% σ_y) at room temperature and 150 °C, respectively. These specimens were subsequently re-shot-peened and fatigued under the previously mentioned testing condition.

The experimental results are shown in Table 4. It can be seen that re-shot peening significantly prolonged the fatigue life of Ti-6Al-4V alloy at both room temperature and 150 °C. This is understandable since re-shot peening could partially or totally restore the subsurface compressive residual stress which was relaxed during the fatigue tests, as shown in Figs. 3 and 4. For the re-shot peened samples cycled at room temperature, the recovered maximum compressive residual stress was closed to that generated by the first round shot peening, 120 ksi (800 MPa), though the thickness of the surface residual stress layer became relatively thinner. However, the re-shot peened Ti-6Al-4V sample fatigued at 150°C, the maximum compressive residual stress was lower, 110 ksi (730MPa) and the surface residual stress layer became even thinner. Re-shot peening is potentially beneficial to the fatigue lives of the components by recovering the relaxed compressive residual stress. However, the benefits are strongly dependent on the percentage of shot-peened life consumed prior to re-shot peening. The effects of shot peening could be detrimental if re-shot peening is performed at stages when the partial fatigue life has exceeded 75% of the shot-peened life.

Table 4 Re-shot peening condition and results (cycles)

N_f (room)	N_{h1} (room)	N_{h2} (room)	N_t (room)	N_f (150 °C)	N_{h1} (150 °C)	N_{h2} (150 °C)	N_t (150 °C)
4.5×10^6	2.25×10^6	4.03×10^6	6.28×10^6	5.5×10^6	2.75×10^6	4.14×10^6	6.89×10^6

N_f— fatigue life at 75% σ_y; N_{h1}—The number of cycles to half of fatigue life before re-shot-peening; N_{h2} — The number cycles to failure after re-shot peening; N_t- The total number of cycles to failure ($N_t = N_{h1} + N_{h2}$).

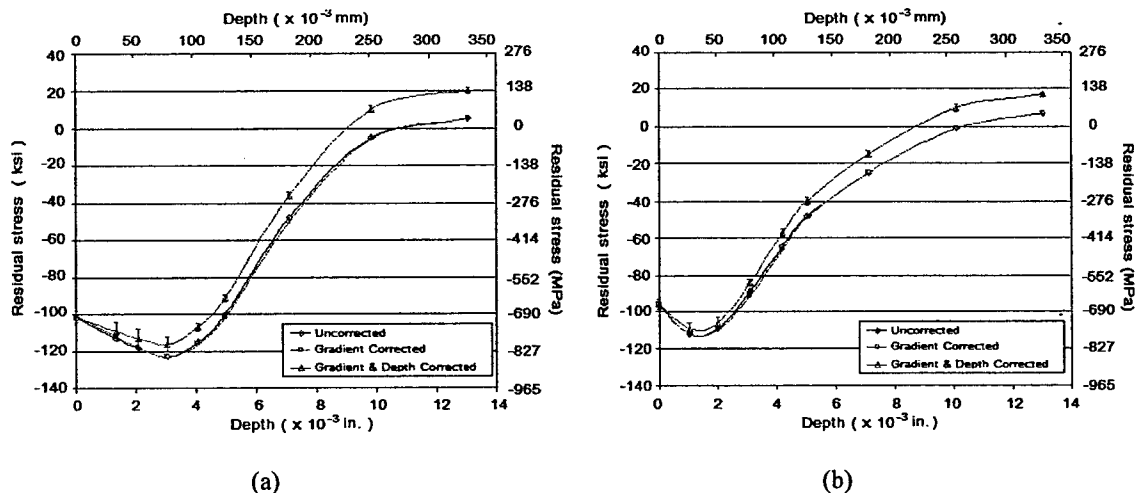(a)   (b)

Fig. 4 Residual stresses of re-peened samples, (a) four-point bend fatigued up to half of its life at room temperature (b) four-point bend fatigued up to half of its life at 150 °C.

Fig. 5(a) shows a surface crack in the as-received Ti-6Al-4V sample fatigued at the applied maximum cyclic stress of 80% σ_y. The crack was initiated in an α phase grain in position "A" in Fig. 5(a). It propagated crystallographically within α-phase grains and noncrystallographically in β-phase grains, which is consistent with previous work on the alloy [14]. Fig. 6 also shows some

crystallographic cracks in α-phase grains in this alloy. As shown in Fig. 5(a), very often only single crack nucleation took place regardless of the applied stress level, unlike many other engineering materials where the number of nucleated cracks is a Weibull function of the applied stress [15]. As shown in Fig. 5(b), the crack grew up faster in α-phase grains than in β-phase grains.
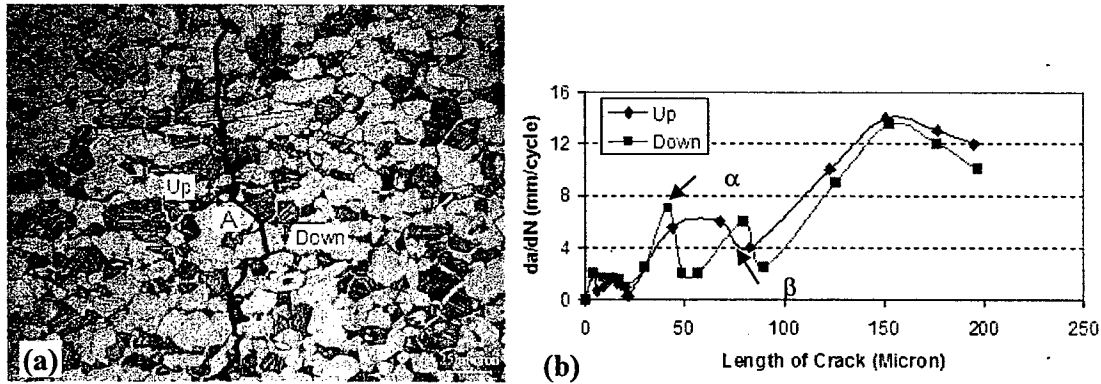

Fig. 5 Growth rate variation of a fatigue crack in a Ti-6Al-4V alloy at 80%$\sigma_{0.2}$.

Fig. 6 shows the fracture crack surfaces of shot peened Ti-6Al-4V samples fatigued at room temperature and 150 °C respectively. The two samples had almost the same fracture behavior, i.e., both have a certain proportion of crystallographic/intergranular fracture in α-phase grains and non-crystallographic fracture in β-phase grains. This demonstrates that the HCF behavior of the Ti-6Al-4V alloy is hardly affected by temperature below 150 °C. The relative area fraction of the crystallographic fracture was in good agreement with that of the α-phase in this alloy. As mentioned above, although fatigue cracks grew faster in α-phase grains, the crystallographic growth in the α-phase grains resulted in rough crack path which could subsequently give rise to so-called roughness-induced closure hence decreasing the crack driving force.
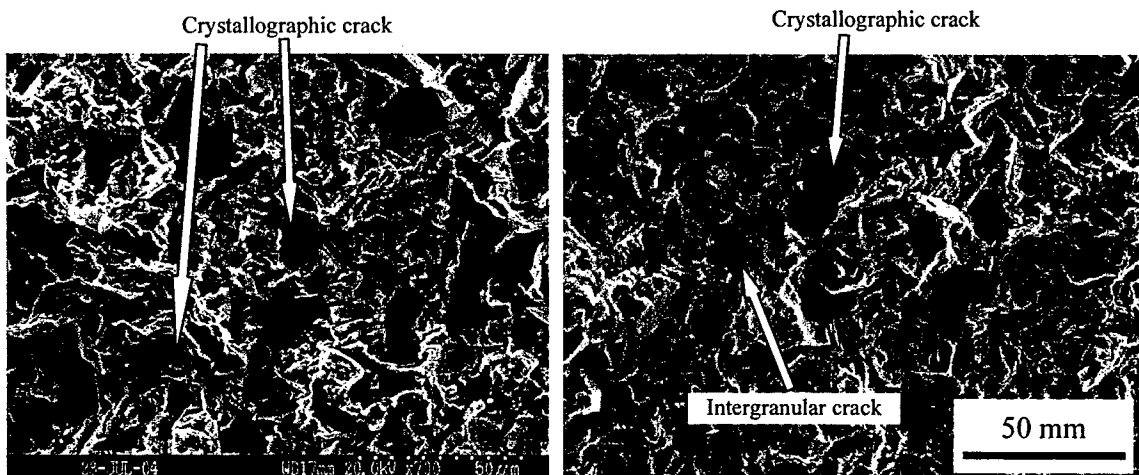
Fig. 6 Fatigue fracture surfaces of shot peened Ti-6Al-4V tested at (a) room temperature, and (b) 150 °C.

3.1.2 Texture

Figs. 7 and 8 are pole figures and orientation distribution functions (ODFs) of the surface of the Ti-6Al-4V alloy before (Fig. 7) and after (Fig. 8) shot peening. By comparing the maximum texture intensity in ODFs between these samples, it can be seen that texture in this alloy was strengthened by shot peening. The main texture components of the as-received Ti-6Al-4V sample were $\{11\bar{2}0\}<1\bar{1}00>$ and $\{0001\}<2\bar{1}\bar{1}0>$. Shot peening produced a plastically deformed layer near the surface, which led to the formation of a basal fiber texture (i.e., $\langle 0001\rangle$//ND fiber) in the layer. This fiber texture has a strengthening effect by the mechanism of orientation hardening. This partially contributed to the enhancement of fatigue strength of shot peened samples, in addition to the residual compressive stress and fine grain structure (as will be discussed in the next section) produced by the peening process. Moreover, this texture strengthening does not easily deteriorate as the residual stress normally does during service. However, it is still desirable to quantify all of the strengthening factors in order to predict the overall effect of shot peening on the fatigue life of a component.
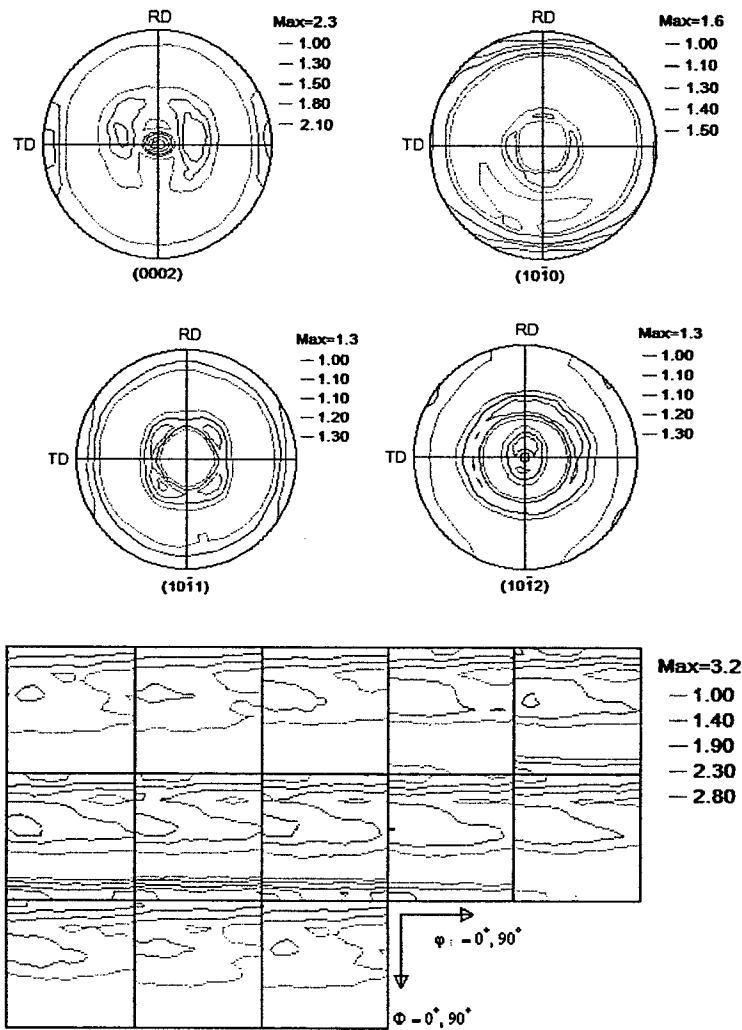
Fig.7 Pole figures and ODF of the as-received Ti-6Al-4V alloy.

24

RD
Max=2.5
— 1.00
— 1.30
— 1.60
— 1.90
— 2.20
TD

(0002)

RD
Max=1.6
— 1.00
— 1.10
— 1.20
— 1.30
— 1.50
TD

(10$\bar{1}$0)

RD
Max=1.4
— 1.00
— 1.10
— 1.20
— 1.20
— 1.30
TD

(10$\bar{1}$1)

RD
Max=1.4
— 1.00
— 1.10
— 1.10
— 1.20
— 1.30
TD

(10$\bar{1}$2)

Max=4.1
— 1.00
— 1.60
— 2.20
— 2.90
— 3.50

$\varphi : - 0^*, 90^*$

$\Phi - 0^*, 90^*$
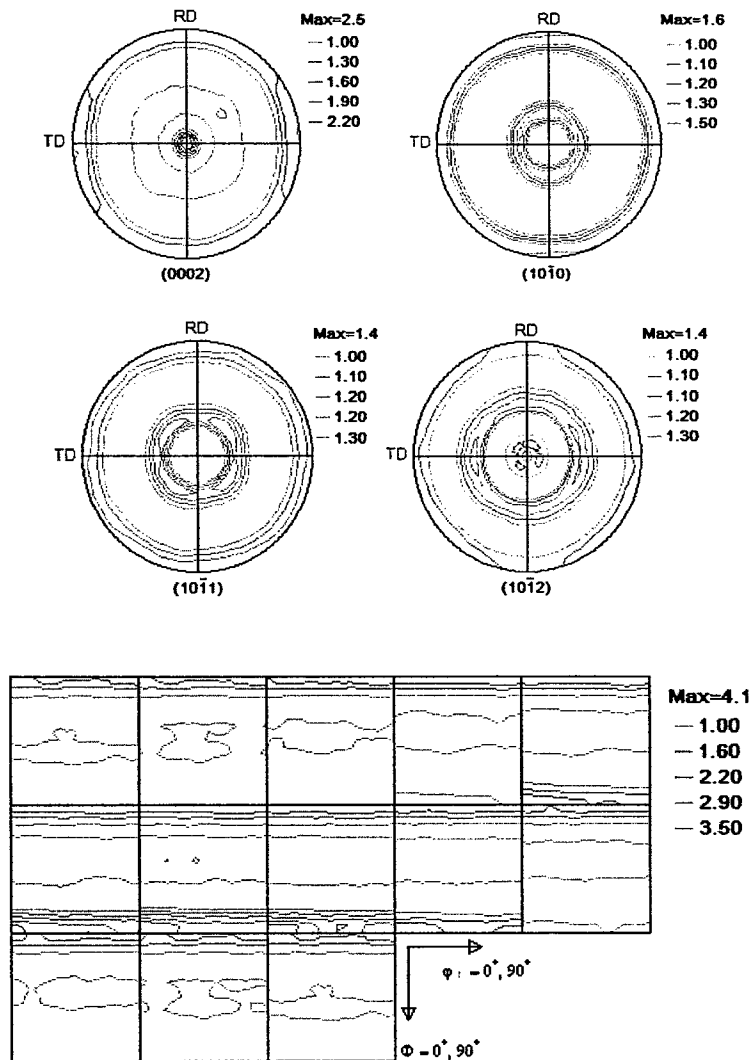
Fig.8 ODF of the shot peened Ti-6Al-4V.

3.2 Sandblasted pure titanium

3.2.1 Surface roughness, microstructure and micro-hardness

Fig. 9 shows the surface roughness of the as-received (Fig. 9(a)) and sandblasted (Fig. 9(b)) pure titanium measured using the Taylor-Hobson Form Talysurf-50 machine. Note that the scale of the vertical axis in Fig. 9(a) is 1/3 of that in Fig. 9(b). The average roughness, Ra, of the sandblasted surface was about 1.1 µm, three times as high as that, 0.3 µm, of the untreated sample. It can be seen in Fig. 9 that some sites in the surface of the sandblasted titanium sheet were as deep as 5 µm from the mean surface line, which was consistent with SEM observations.

(a)

(b)
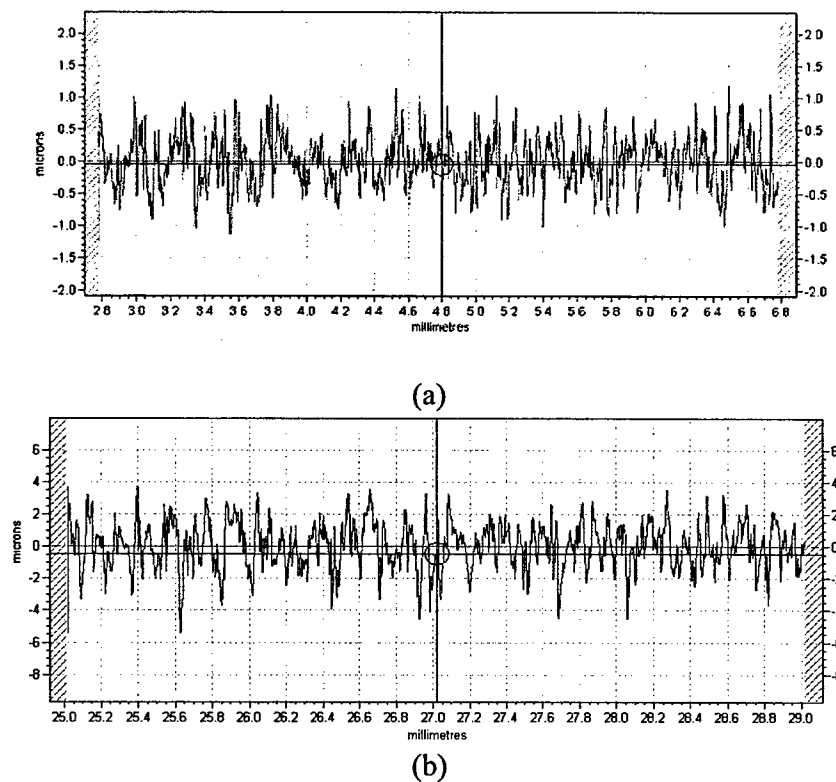
Fig. 9 Surface roughness of the (a) untreated titanium, (b)sandblasted titanium.

Fig. 10 is the micrograph showing the cross-section of the sandblasted specimen. Three different regions were observed in the sample, i.e., the severely deformed surface layer, the region deformed by mainly twinning and the un-deformed substrate. From the figure, thickness of the first two regions was about 70 micron. They were likely to be responsible for the enhancement of the fatigue properties, since they showed fracture characteristics profoundly different from that of the substrate in fatigue test. After annealing at low temperature, a nanocrystalline structure was formed in the surface layer of these sandblasted samples, and its corrosion resistance was significantly improved.
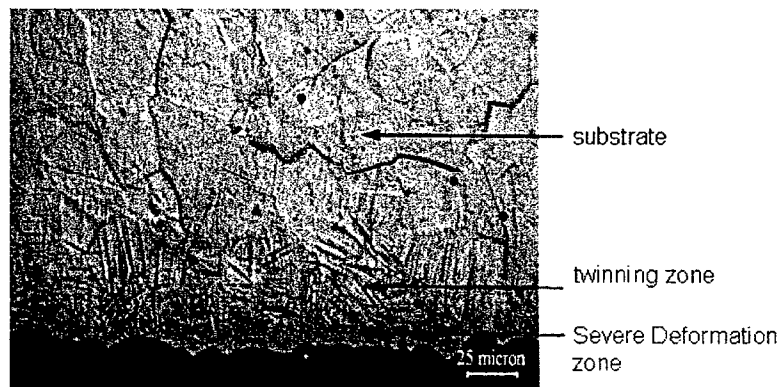
Fig. 10 Microstructure of sandblasted titanium sheet

In sandblasting, twinning was the predominant deformation mode in the region below the severely deformed surface layer. It can be seen in Fig. 10 that twins were formed in grains in region 2. Since the limited number of slip systems of hexagonal closed packed metals, dislocation slip and deformation twinning were the two principal modes of plastic deformation. Normally, the deformation modes in hexagonal crystals have the followed three slip systems and one twinning system [16]: 1) basal $\{0001\}\langle11\bar{2}0\rangle$; 2) prismatic $\{10\bar{1}0\}\langle11\bar{2}0\rangle$, 3) pyramidal $\{11\bar{2}2\}\langle11\bar{2}\bar{3}\rangle$, $\{10\bar{1}1\}\langle11\bar{2}0\rangle$, and 4) twinning $\langle10\bar{1}0\rangle$ slip on $\{10\bar{1}2\}$. Twinning contributed to plastic deformation by the shear it produced. More importantly, the twinning process served to reorient the crystal lattice to favor further basal slip.

Fig. 11 is the profile of micro-hardness measured in the sandblasted titanium. In the sandblasted samples, hardness was highest in the severely deformed near surface layer. Hardness decreased significantly with increase in depth, which coincided with the residual stress profile measurement and microstructure observed in these samples. The hardness dropped from 240 HV at 10 μm to 194 HV at 20 μm. After recovery heat treatment, hardness was decreased, compared to that of the as-sandblasted sample. However, the decrease in hardness was moderate with increase in depth. Below 40 μm, the hardness remained constant and they were close in values (only varying from 142 HV to 153 HV) at 60 μm for all the different samples, i.e., as-sandblasted and sandblasted-annealed at 200 °C, 250 °C & 300 °C, respectively.
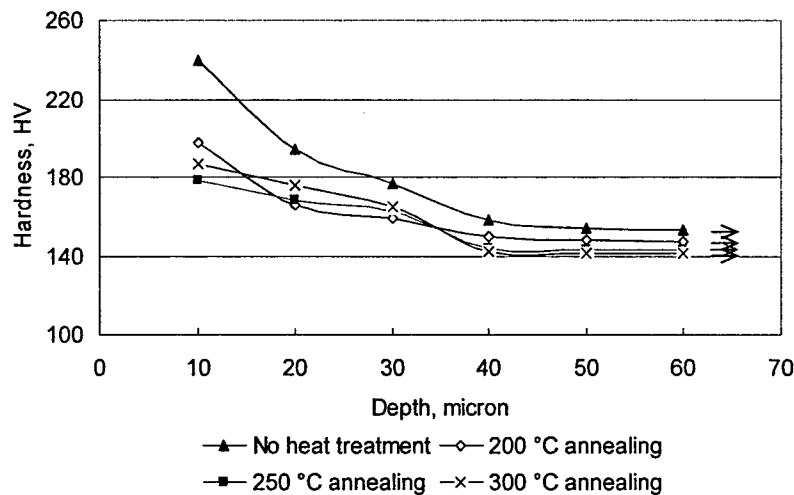

Fig. 11 Micro-hardness of sandblasted titanium

3.2.2 Residual stress and fatigue properties

The profile of the residual stress in the sandblasted surface layer was measured by the X-ray diffraction technique, as shown in Fig. 12. The sandblasting induced compressive residual stresses were confined to a shallow surface layer, within ~70 μm of the surface, while low compensatory tensile residual stresses spread deeper through the cross-section. The compressive residual stress reached the maximum 480 MPa at about 10 μm below the surface.
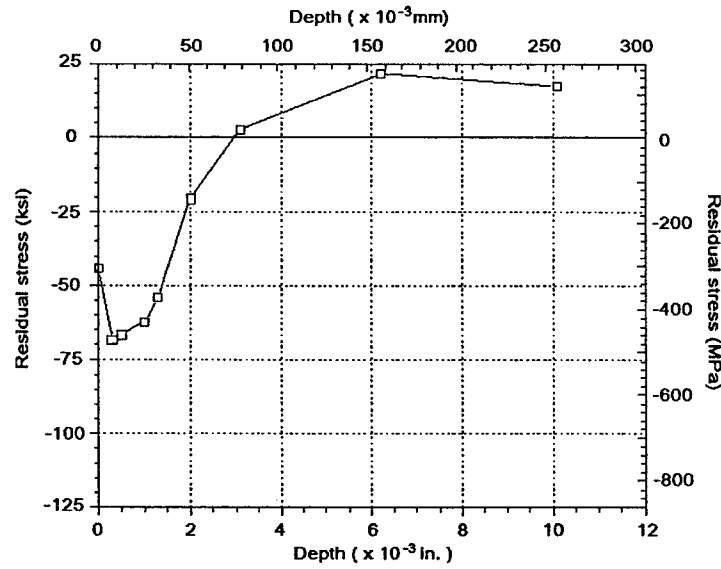
27

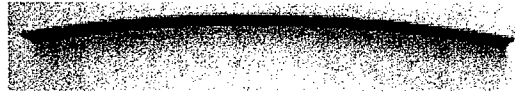Fig. 12 The profile of residual stress of sandblasted titanium.

Fig. 13 The titanium sheet after sandblasting.

The sandblasting generated a thin layer of compressive residual stress on one side of the titanium sheet, which bent the sheet as shown in Fig. 13. With the thickness of the compressive layer known, the average compressive stress could be estimated from the measurement of the curvature $(1/R)$ of the sample sandblasted on only one side. If we model the compressive layer as an isotropic "thin film" with equi-biaxial stress σ_c and thickness δ, which is rigidly attached to an initially stress-free isotropic "substrate" of thickness h, the average equi-biaxial stress in the compressive layer can be estimated by using the following modified Stoney formula [17]:

$$\sigma_c = -\frac{Eh^2}{6(1-v)R\delta},\qquad(3)$$

where E is the Young's modulus and v the Poisson ratio of the "substrate". Here, with $h = 0.73$ mm, $R = 420$ mm, $\delta = 0.07$ mm, $E = 120$ GPa, and $v = 0.3$, the residual compressive stress is calculated to be $\sigma_c = -494$ MPa, which is in good agreement with the result measured by the X-ray method. This calculation would be valid only when the thickness of the compressive stress layer was known. Otherwise, there could be many stress conditions that would result in the same curvature of the sheet.
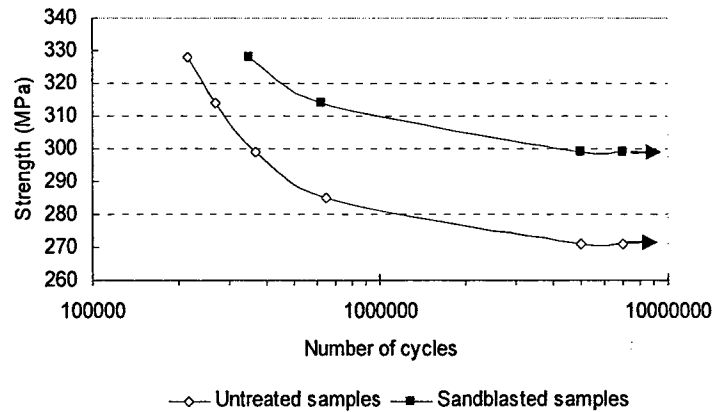
28

Fig. 14 S-N curves of pure titanium before and after sandblasting.

Fig. 14 shows the measured S-N curves of titanium before and after sandblasting. The fatigue limit of untreated titanium was about 270 MPa, while it was about 300 MPa for the sandblasted titanium. Compared with that of the untreated Ti samples, the fatigue strength of sandblasted Ti samples was increased by about 11%. As discussed later in this report, sandblasting induced not only the compressive residual stress, as well as formation of a $\langle 0001 \rangle$//ND fiber texture and fine grains in the surface layer. The increase in fatigue strength, therefore, was due to the existence of the residual stress, orientation hardening and grain refinement in the surface layer.

(a)   (b)

(c)   (d)
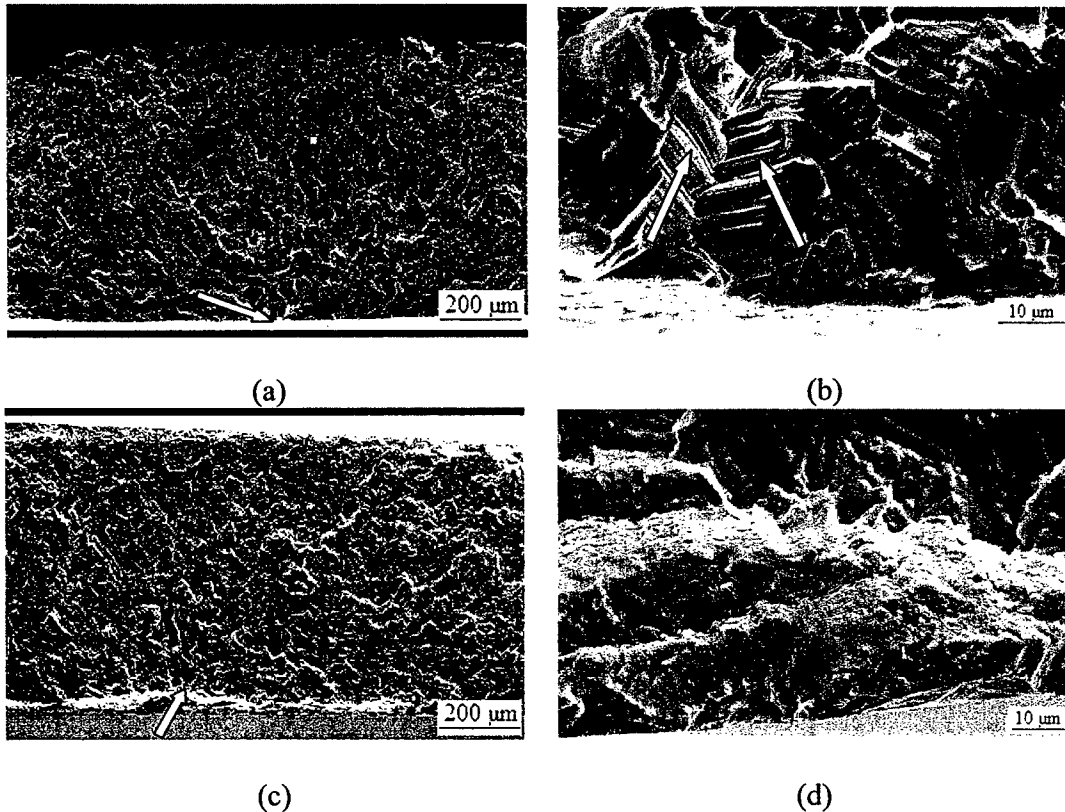
Fig. 15 SEM micrographs showing the fatigue fracture surfaces of titanium (a) (b) before, and (c) (d) after sandblasting.

29

Fig. 15 shows the SEM micrographs of the fatigue fracture surfaces of the sandblasted and as-received titanium. In the as-received titanium, the crack was initiated on the surface of the specimen (Fig. 15(a)), and short crack growth was mainly crystallographic (Fig. 15(b)). In contrast, in the sandblasted Ti, the fatigue crack was initiated in the subsurface due to the compressive residual stress in the surface layer (Fig. 15(c)), and crack growth in the surface layer was almost featureless (Fig. 15(d)). This meant that the combination of the compressive residual stress, extremely fine grains and ⟨0001⟩//ND fiber texture was effective in preventing crack initiation on the surface, in despite of the surface becoming rougher.

3.2.3 Grain size measurement

Some of the sandblasted Ti samples were recovery treated at 200 °C, 250 °C and 300 °C, respectively. An X-ray diffraction method was adopted to measure the grain size of these samples annealed at 200 °C. The detailed slow XRD scans of 2θ were performed (degree) from 45.7 to 48.4, 60.5 to 63.7 and 82.6 to 85.6 respectively. The following equations were used to calculate the grain size L in this study [18].

$$\delta(2\theta) = B\left(1 - \frac{b^2}{B^2}\right) \quad \text{(radian)} \tag{4}$$

$$L = \frac{k\lambda}{\delta(2\theta)\cos\theta_0} \tag{5}$$

where $\delta(2\theta)$ is instrumental broadening-corrected breadth; B and b are the breadths of the same Bragg peak from the XRD scans of the experimental and reference sample; k is a constant, roughly equal to 0.9; λ is the wave length and θ_0 is the position of the analyzed peak.

A titanium sample annealed at 600 °C for 30 min was used as the reference sample. The peak of the sandblast-annealed sample was broadened in XRD experiment, compared with that of the reference sample, as shown in Fig. 16.
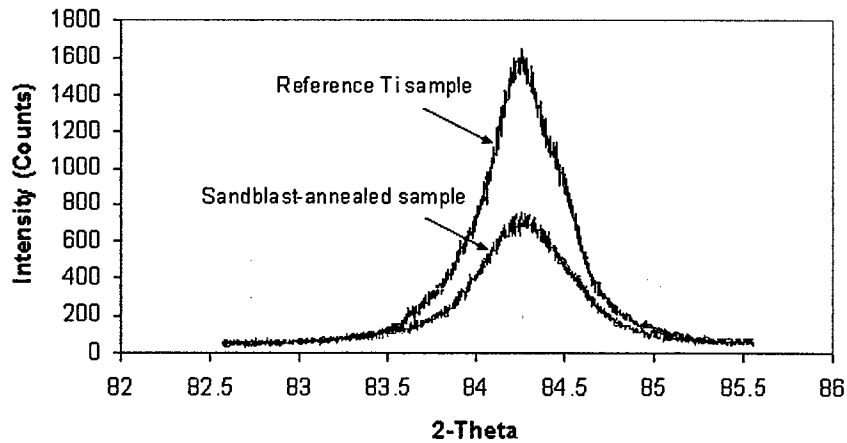

Fig. 16 XRD spectra of reference and sandblast-annealed Ti samples

30

Table 5 is the full width at half maximum (FWHM) results of experimental and reference samples. It is evident in table 5 that the FWHMs of sandblast-annealed titanium were larger than that of reference titanium sample. The grain size of the sandblasted titanium after annealing at 200 °C was around 50 nm [19]. Note that the peak broadening is usually contributed by decreasing grain size and increasing dislocation density. This XRD result is more or less affected by dislocation density but the influence is minor since the specimens were annealed at low temperature.

Table 5 FWHMs of different measured peaks.

Samples	Centroid (2θ, degree)	FWHM (degree)
Reference Ti	84.359	0.372
Sandblast-annealed Ti	84.260	0.500
Reference Ti	62.345	0.320
Sandblast-annealed Ti	62.428	0.448
Reference Ti	46.936	0.318
Sandblast-annealed Ti	46.903	0.420

3.2.4 Electrochemical property

In order to evaluate the corrosion resistance of the as-received, sandblasted and sandblasted-annealed titanium, corrosive immersion tests were carried out. The samples were mounted in epoxy to expose only one surface for the electrochemical tests. The polarization behavior was studied in a 3.5% NaCl solution at a potential scanning speed of 20mV/min. A saturated camel electrode (SCE) was used as the reference electrode and a platinum wire was used as the counter electrode. All electrochemical tests were carried out at room temperature.

The results indicated that the sandblast-annealed sample has the highest resistance to corrosion in a salt solution, as shown in Fig. 17. The potentiodynamic polarization curves showed that the sandblast-annealed titanium had the lowest i_{corr}, corrosion current density, and passivation current (making the intersection points of the tangents of the upper and below sides of the curves, the corresponding X axial values were the corrosion current density). These passivation results were influenced by the formation of oxide on the metal surface in a certain range of potential. A thin passive film could restrict the movement of metal ions from the metal surface to the solution, thus minimizing corrosion. In the surface nano-crystalline layer, the high density of grain boundaries was beneficial to the formation of passive film, which accounted for the improvement of the polarization behavior of the sandblast-annealed titanium.
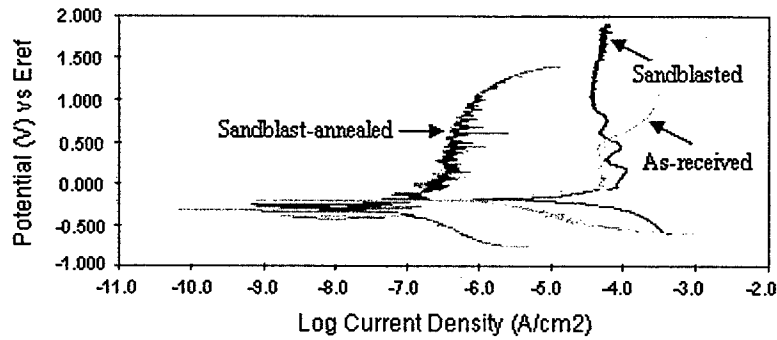
31

Fig. 17 Polarization curves of different specimens in a 3.5% NaCl solution.
Scanning rate: 20mV/min

Generally, the performance of a passive film is affected by the interfacial bonding between the film and the substrate [20]. For the sandblasted titanium, the interfacial bonding between the passive film and substrate becomes weaker because the high density of dislocations in the vicinity of the interface could weaken the oxide/Ti interface, compared with that of the sandblast-annealed sample. The weaker interfacial bonding, the poorer polarization performance.

3.2.5 Texture

Fig. 18 is the ODFs of titanium before and after sandblasting. Fig. 19 is (0002), $(10\bar{1}0)$ pole figures of titanium before and after sandblasting. The as-received titanium had a much higher intensity of texture than that of the sandblasted sample. The main texture components of untreated titanium were $\{11\bar{2}0\} < 0001 >$ $(90°, 90°, 30°)$, $\{11\bar{2}4\} < 1\bar{1}00 >$ $(0°, 37°, 30°)$. The (0002) poles were tilted towards TD and the $(10\bar{1}0)$ poles were parallel to RD, which were similar with the simulated pole figures as reported in [16]. The crystallographic orientation has a $30°$ tilt away from the normal direction to both two transverse directions, which result from the combination of prismatic $\{10\bar{1}0\}\langle 1\bar{1}\bar{2}0\rangle$ slip and basal $\{0001\}\langle 1\bar{1}\bar{2}0\rangle$ slip in titanium. This kind of texture was called Transverse texture (T-texture), which was usually observed in ideal rolling condition.
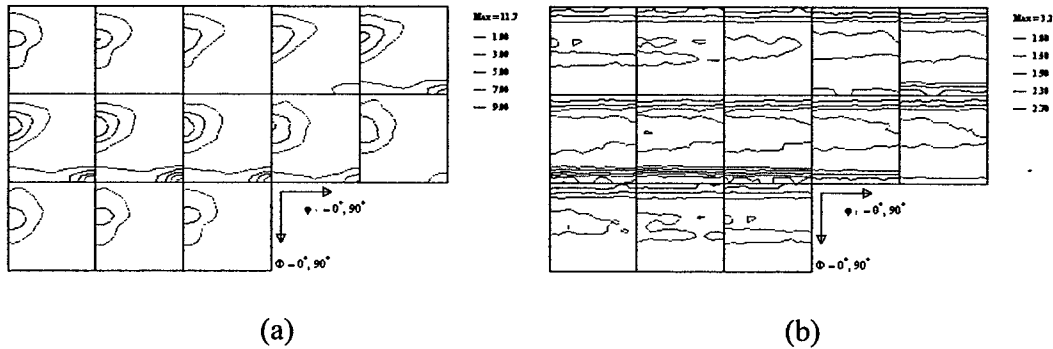

(a)   (b)

Fig. 18 Constant φ_2 ODF sections of titanium (a) before, and (b) after sandblasting

(a) (0002)   (b) (10$\bar{1}$0)

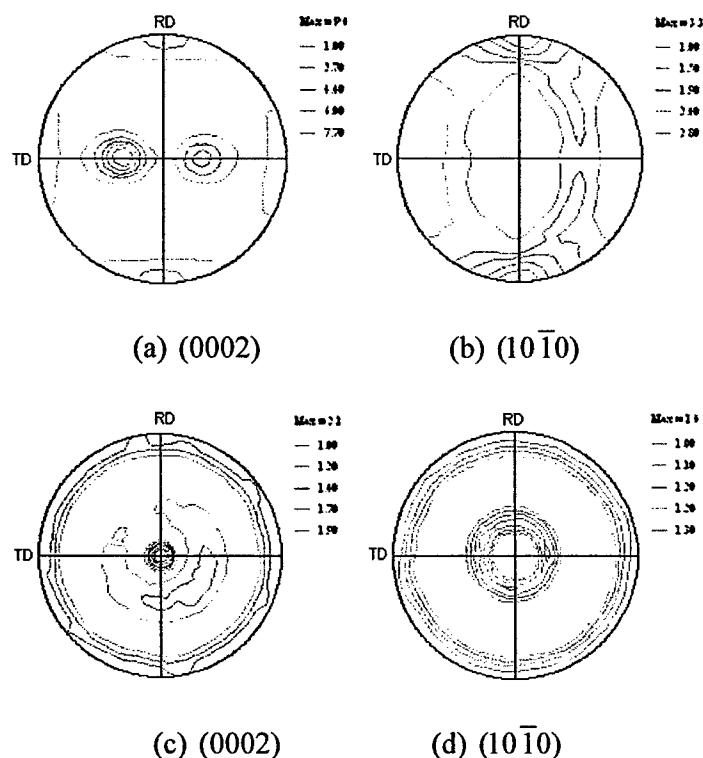(c) (0002)   (d) (10$\bar{1}$0)

Fig. 19 Pole figures of titanium (a) (b) before, and (c)(d) after sandblasting.

In the sandblasted titanium, a near surface plastic deformation zone generated due to the sand particles repeatedly impacted the sample surface. Within the plastically deformed layer, crystallographic texture was changed. Sandblasting not only decreased the intensity, but also changed the texture component completely. A basal fiber texture formed after sandblasting (B-texture). As we discussed before, the deformation mode in hexagonal materials was base on three slip system and one twinning system. In spite of the large number of publications on deformation systems in titanium and on deformation texture evolution, it was still unclear that which system dominated the B-texture formation, the <c + a> dislocations or twinning. During sandblasting processing, the local deformation initially weakened the original T-texture component and active mechanical twin, which led to the formation of B-texture.

3.3 The Effects of micro- and macro-texture on fatigue properties in AA 2026 Al alloys

3.3.1 Crack initiation

In these alloys, fatigue cracks are always initiated from Fe-containing coarse particles as shown in Fig. 20 [7]. These particles contain Al, Cu, Fe and Mn and appear to be relatively brittle, since cracks are never formed from other types of coarse particles, such as s-phase (Al$_2$CuMg) and θ phase Al$_2$Cu in these alloys. As shown in Fig. 20(c), not all the micro-cracks from the particles can propagate into the matrix, because the neighboring grain has to provide a slip plane, which forms a small twist angle with the micro-crack in the particle, for the micro-crack to propagate into the grain. Since the micro-crack is almost always perpendicular to both the stress axis and

33

sample surface, the grains which can provide a slip plane with a smallest twist angle for the crack to propagate onto are those grains belong to the $\langle 100 \rangle //L$ fiber texture. Typically the grains with the recrystallized texture such as cube $\{001\}\langle 100 \rangle$ and Goss $\{011\}\langle 100 \rangle$ are among these orientations. Since these alloys possess about 90% the unrecrystallized and only 10% recrystallized grains, there is only about 10% chance for a micro-crack to propagate into its neighboring grains at the most. As a result, the number of fatigue weakest-links, i.e., the potential crack nuclei, is even smaller, as the number of coarse particles in these alloys is far less than that in the traditional AA2024 alloy. This is part of the reason why the fatigue limit of the AA 2026 alloys is so much higher than that of AA2024 alloys. In this work, because of the difficulty in etching and electropolishing the 2026 alloys, measurement of the twist angles between the retarded micro-cracks in particles and the possible slip planes in the neighboring grain had not been successfully conducted by EBSD. Further work still needs to be done to verify the above proposed mechanism for micro-crack retardation in particles in 2026 Al alloys.
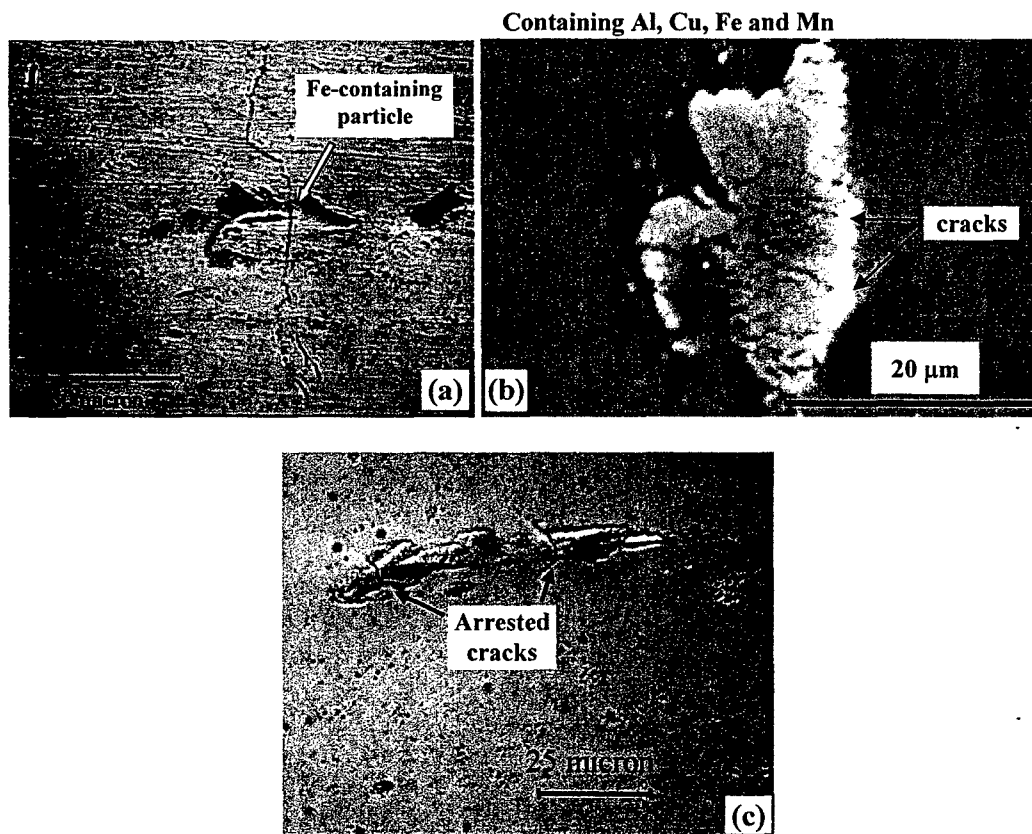
Containing Al, Cu, Fe and Mn

Fig. 20 Crack initiation from coarse particles in a) square bar, stress level 100% σ_y, 1.5×10^5 cycles and c) rectangular bar, stress level 100% σ_y, 1.7×10^6 cycles.

Multiple crack initiation was often observed, especially when the stress level was well-over the fatigue limit in the 2026 alloys [15]. With increasing in the applied stress level, the number of the cracks initiated from the cracked particles was also increased. It was found that the number (N) of cracks was a Weibull function of the maximum stress ranging up to the ultimate tensile stress, as shown in Fig. 21(a),

$$N = N_0 \left(1 - \exp\left[-k\left(\frac{\sigma - \sigma_0}{\sigma_0} \right)^m \right] \right) \qquad (6)$$

where

> N_0: the number of cracks in the surface area of 10×6 mm^2 at the stress level close to the ultimate tensile strength (σ_s), i.e., weakest link density ($N_0/(10×6$ mm$^2)$).
> k: constant,
> m: Weibull modulus,
> σ_0: fatigue limit

N_0 and σ_0 can be determined experimentally from S-N curve measurement, since,

> $\sigma \leq \sigma_0$, $N = 0$, and,
> $\sigma \geq \sigma_s$, $N = N_0$, i.e., N_0 is approximately the number of fatigue cracks that can be initiated at $\sigma \geq \sigma_s$ (ultimate tensile strength).

Equation 6 is the crack population observed at a cyclic stress level. By taking derivative of Equation 6, the strength distribution of fatigue weakest-links can be derived:

$$n = CN_0 \left(\frac{km}{\sigma_0} \right)\left(\frac{\sigma - \sigma_0}{\sigma_0} \right)^{m-1} \exp\left[-k\left(\frac{\sigma - \sigma_0}{\sigma_0} \right)^m \right], \qquad (7)$$

where n is the number of the fatigue weakest-links that have a fracture strength of σ, and C is a scaling constant which can be determined by

$$N_0 = \int_0^{+\infty} n\,d\sigma. \qquad (8)$$

C depends on the unit of σ used in Equation 7. Both N_0 and n can be regarded as materials properties with N_0 being the density of fatigue weakest-links (since the total surface area under the maximum applied stress is known in this work) and n being the characteristic strength distribution of fatigue weakest-links in materials. Fig. 21(b) shows the strength distribution calculated from Fig. 21(a). The weakest link distribution could be related to the strength distribution of the possible microstructural inhomogeneities, such as inclusions, particles, grain and phase boundaries, non-uniformity of composition and precipitate distribution, and strain concentrations (such as persistent slip bands, etc.), etc., in an alloy. It has long been recognized that fatigue crack initiation take place from these inhomogeneities in metallic materials. These inhomogeneities could lead to fatigue cracks at different cyclic stress levels, i.e., their strength, and therefore, are referred as fatigue weakest links. By measuring the number of cracks at different cyclic stress levels, the strength distribution of the weakest links can be determined, assuming that one crack is only associated with one crack initiation site in this alloy. This distribution is a materials fatigue property and of value for both materials producers and engineering designers. For a material with a better fatigue performance, N_0 should be as small as possible, n as narrow as possible and the stress of its peak should be as high as possible.
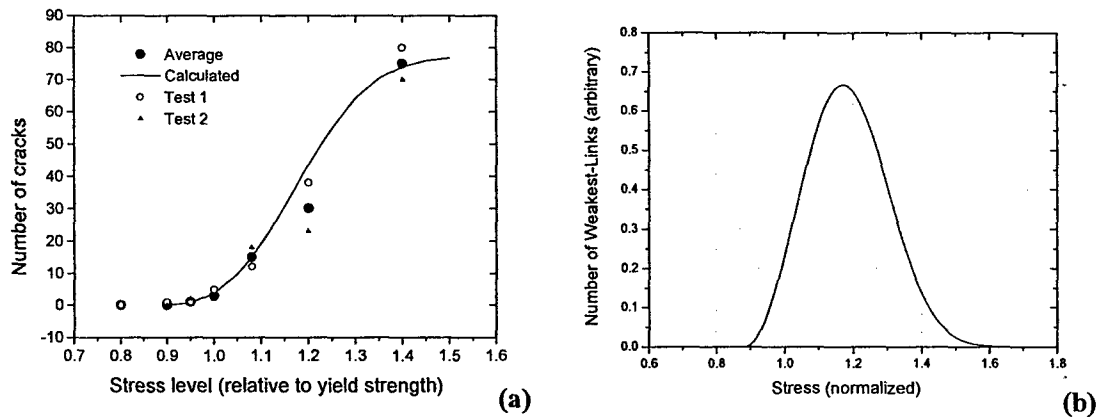
Fig. 21 (a) Experimental and calculated crack population vs. stress plot. And (b) strength distribution of fatigue weakest-links in the AA 2026 Al-Cu alloy.

3.3.2 Crack propagation

Fig. 22 shows the typical crack morphology and the growth rate of the crack in the rectangular bar 2026 alloys. The growth rate of the crack is measured by monitoring the crack length projected to the direction perpendicular to the loading axis and plotted against the crack tip position, so that the growth rate in different regions of the crack can be compared. The applied stress level was 120% yield strength. It can be seen from Fig. 22 that there are two types of characteristic crack morphologies, one (non-crystallographic) is in a zigzag shape and perpendicular to the load axis and the other (crystallographic) is straight and runs in a direction of about 35° to the load axis. The early growth of a crack is almost always perpendicular to the load axis, and the rest of the crack grows predominantly along 35° to the load axis. The crack growth rate in the perpendicular growth regions is much slower, about 10 nm/cycle, than that (38 nm/cycle) in the 35° growth regions.

Like other planar slip alloys, these 2026 Al alloys also demonstrated predominantly crystallographic characteristics of crack growth, except in the regions that contained patchy distribution of non-shearable particles/precipitates. A crack always preferably propagated along a certain crystallographic plane within each grain. In Al-Li alloys, it has previously been verified by means of electron back scatter diffraction and acoustic microscopy that the preferred crystallographic plane for crack growth is a {111} slip plane [6]. Although the orientation of the preferred crack plane was not identified in this work, it was likely also to be along a {111} slip plane in 2026 alloys
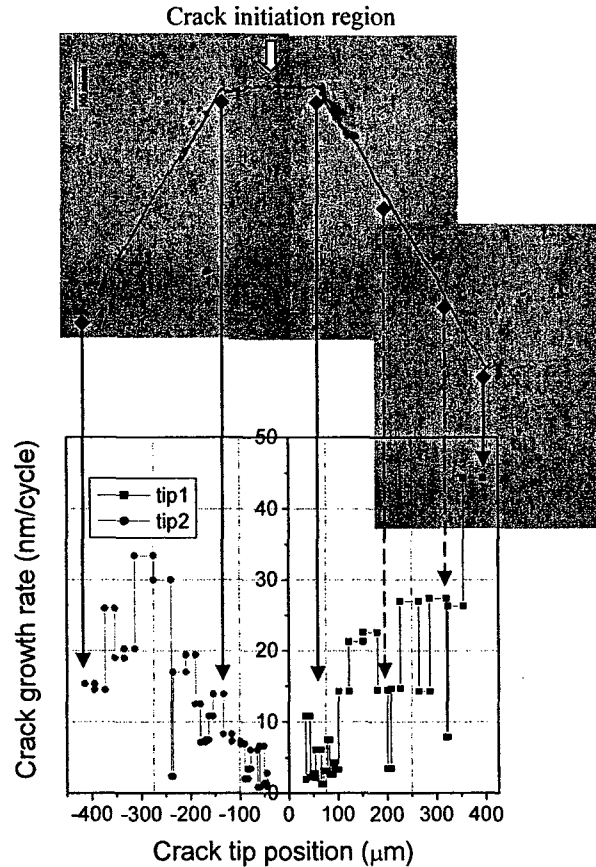
36

Fig. 22 The growth rate of a short fatigue crack in the L-T direction of the rectangular extrusion sample. The maximum stress was 120% σ_y.

The 2026 square extrusion bar had much coarser grains (fibril in shape and 100 μm across) than those (layered and 20 μm in thickness) of the rectangular bar, which may be responsible for the slightly lower fatigue strength measured for the square bar samples. The fatigue fracture topographies of the two extrusion bars were markedly different. Fig. 23 shows the typical fatigue fracture surface of a rectangular bar sample at low magnifications. Regions A and B as marked in Fig. 23(a) correspond to the regions of crystallographic and non-crystallographic crack growth respectively. On average, region B was about 10% in volume fraction in this alloy. Figs. 23(b) and (c) are the fracture surfaces at a higher magnification in regions "A" and "B" respectively. It can be seen that the crack deflected at every grain boundary that had interacted with the crack in the rectangular sample. Grain boundaries were straight and very long. Grains were about 20 μm thick. In the crystallographic growth region (Fig. 23(b)), fracture steps on the crack plane were small within each grain, whereas they were large in the non-crystallographic growth region (Fig. 23(c)). In comparison, the perpendicular growth regions that contained bands of non-shearable particles/precipitates, e.g., in the crack initiation region, did not show the features of crystallographic fracture in these alloys (Fig. 22). The formation mechanisms for the two types of perpendicular crack growth should be different.
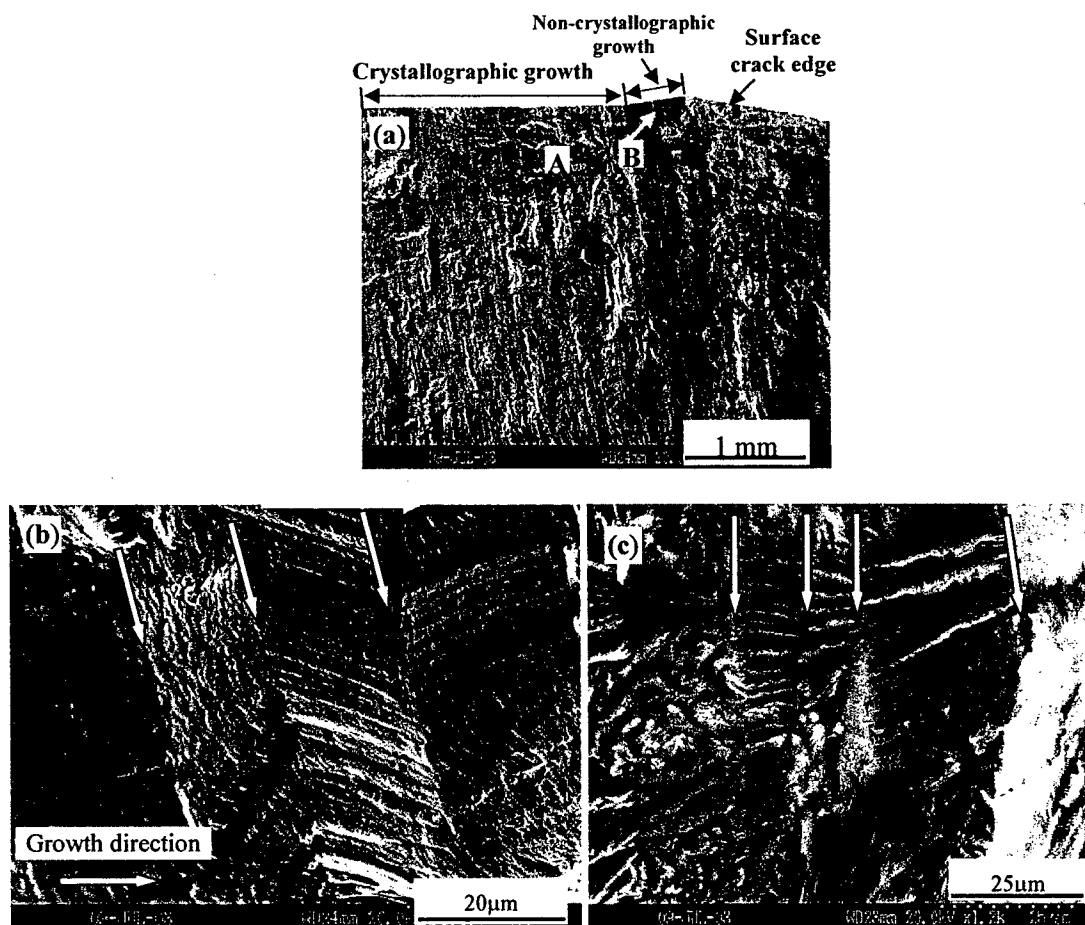
Fig. 23 Fractography of the rectangular extrusion sample. a) at a low magnification, b) Crystallographic crack growth region from region "A" in a), and c) Non-crystallographic crack growth region from region "B" in a). Stress level: 108% σ_y at 2.5×10^5 cycles (arrows indicate the crack growth direction and grain boundaries respectively).

According to the crystallographic model discussed earlier [6], the larger the fracture steps on the crack plane within each grain, the larger the twist angle of the crack plane deflection across a grain boundary. In other words, in the crystallographic growth region, crack plane was always deflected by a smaller twist angle across a grain boundary, while it has a relatively large twist component of the deflection across the boundary in the non-crystallographic growth region. This indicated that, in region A, grain boundaries had a resistance to crack growth much lower than that in region B, which was consistent with the crack growth rate measurement that cracks grew faster in region A than in region B in this alloy (Fig. 23). As discussed later in the report, region A and B were associated with unrecrystallized and recrystallized regions in the alloy.

Fig. 24(a) shows the typical fracture topography of a square extrusion sample; drastically different from that of the rectangular extrusion sample. The cracks were still deflected frequently, and fracture steps were also observed straight and parallel to each other within different regions. However, the boundaries where these fracture steps were originated were not well defined, unlike in the rectangular extrusion samples. This type of fracture behavior is likely to be related to the coarse fibril grain structure in the square bar samples. As illustrated in Fig.

38

24(b), assuming that the grain structure consists of fibril grains with a hexagonal cross-section, the grain structure on the cross-section along the crack path in the direction of 35° relative to the loading axis, i.e. along the plane parallel to the fracture plane parallel lines *AB* and *BC* in Fig. 24(b), would appear as shown in Fig. 24(c). The grains on this cross-section are elongated in the direction of crack growth, which resembles, to certain degree, the fracture topography in terms of the orientation, shape and size of fracture elements in Fig. 24(a). This indicates that the grain structure played a significant role in crack growth in this alloy, since different grain structures resulted in different fatigue fracture topographies.
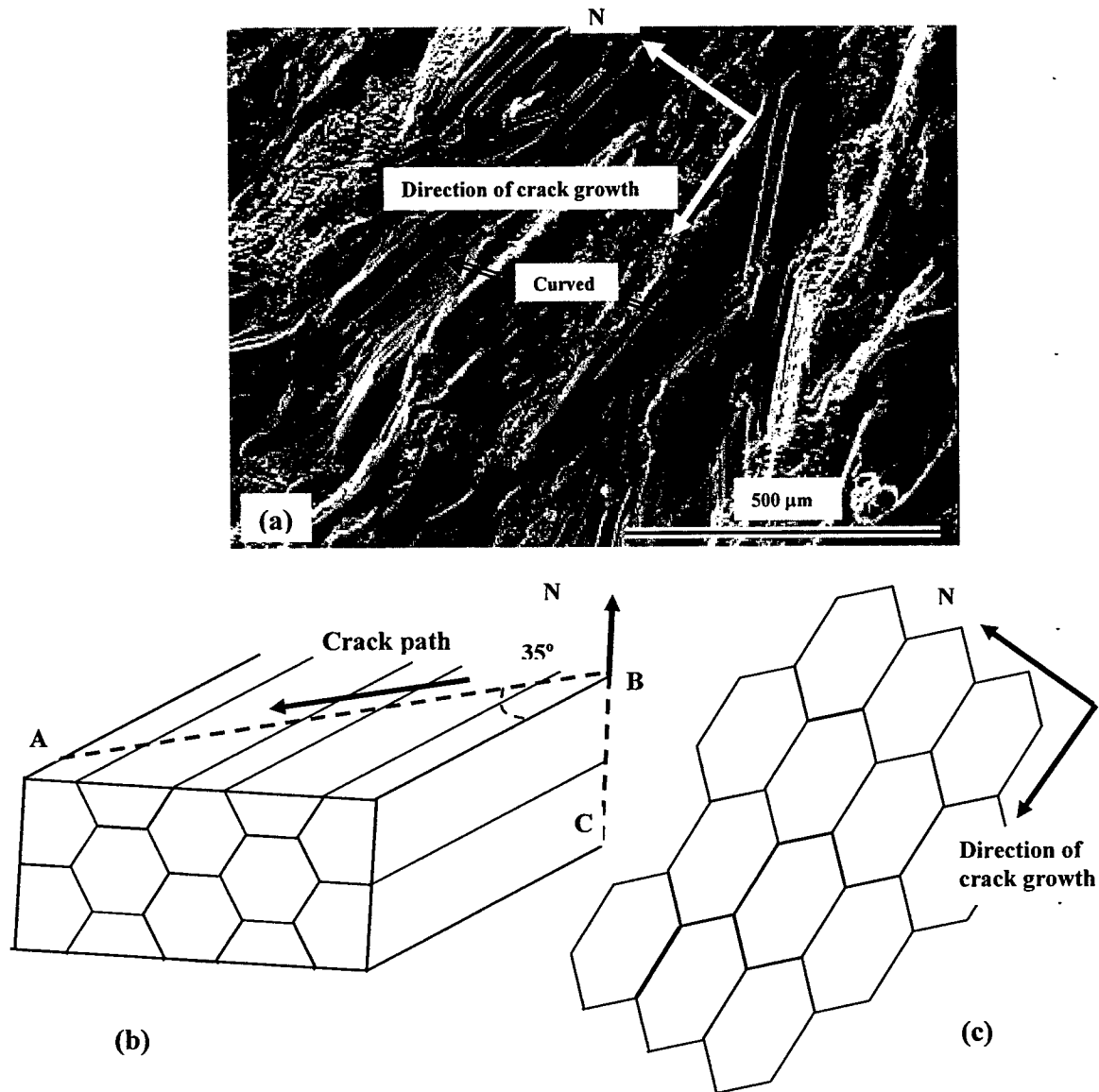
Fig. 24 (a) Fractography of a square extrusion sample, (b) Schematic diagram of the fibril grain structure (with a uniform grain size) in the sample, and (c) schematic diagram of the grain structure on the cross-section along the crack path in the direction of 35° relative to the extrusion direction

If each region where fracture steps were parallel is assumed to be equivalent to one grain in the square extrusion, the diameter of the fibril grains in this alloy can then be estimated to be 125 μm from the fracture topography in Fig. 24(a). This value is similar as that (about 100 μm) measured from the optical micrograph of this alloy. However, within grains the crack plane was often not flat, which was possibly caused by crack deflection inside these grains due to the existence of multiple grain boundaries around them. Fig. 25 is an example of the crack deflections at a GB triple junction and inside grains. These interior and multiple crack deflections could increase the resistance to crack growth, which might partially account for the excellent high cycle fatigue strength of the square bar samples (though it was still slightly lower than that of the rectangular bar), and its slower crack growth rate than that of the rectangular extrusion, as reported in [8], despite of the fact that the square bar had a much coarser grain structure.
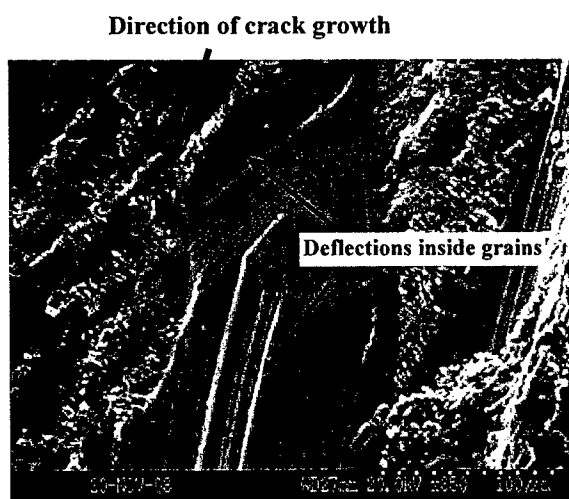
Direction of crack growth

Fig. 25 Crack deflections at a grain boundary triple junction and inside grains in the square extrusion sample.

3.3.3 Electron back scatter diffraction

It appeared that the AA2026 alloy could not yield a damage-free surface finish by electropolishing for the purpose of electron back scatter diffraction experiment. Therefore, an AA2099 Al-Li alloy was chosen as an alternative alloy for studying the relation of texture to the crack growth behavior in planar slip alloys. The 2099 alloy was produced using a similar processing procedure as that for the AA 2026 alloy, and it also had a similar layered grain structure as in the AA2026 alloy. The AA2099 alloy was relatively easier to be electropolished and etched to produce damage-free surface, as shown in Fig. 26(a). As in the AA2026 alloy, two different regions were observed on the specimen surface of the 2099 Al alloy, i.e., region A of crystallographic growth and region B of non-crystallographic growth (Fig. 26(a)). Grain orientations of these regions were determined using electron back scatter diffraction technique. The results revealed that region A in Fig. 26(a) was recrystallized with a typical strong cube texture, as shown in the ODF in Fig. 26(b), and that region B in Fig. 26(a) was non-recrystallized with a typical rolling texture as demonstrated in the ODF in Fig. 26(c). The crack path on the surface was roughly in the direction of 35° with the loading axis in the specimen. As discussed later in the report, the unrecrystallized region had far more grain boundaries with a crack plane twist angle below 5° than those in the recrystallized region. This was consistent with the fracture observation that a crack was predominantly deflected by a small twist angle across grain

boundaries in the unrecrystallized region and by a large twist angle across grain boundaries in the recrystallized region. Although the recrystallized regions covered only about 10% area in the specimen, it provided large twist of crack plane deflection at grain boundaries, i.e., large resistance to crack growth.

(a)
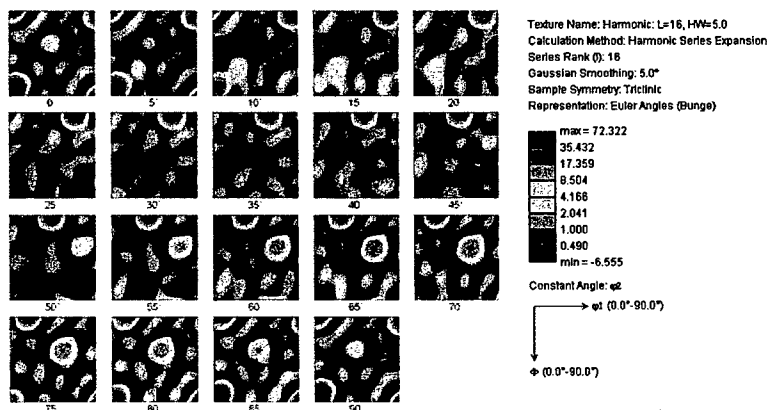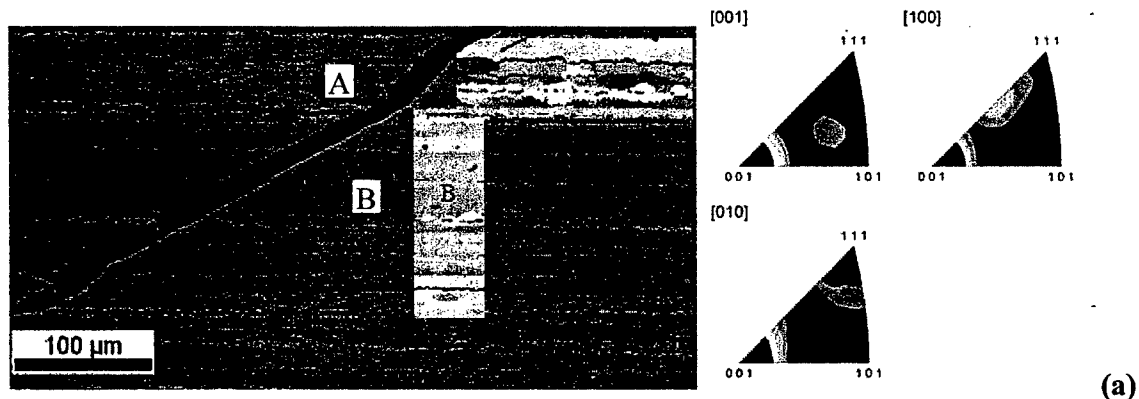
(b)
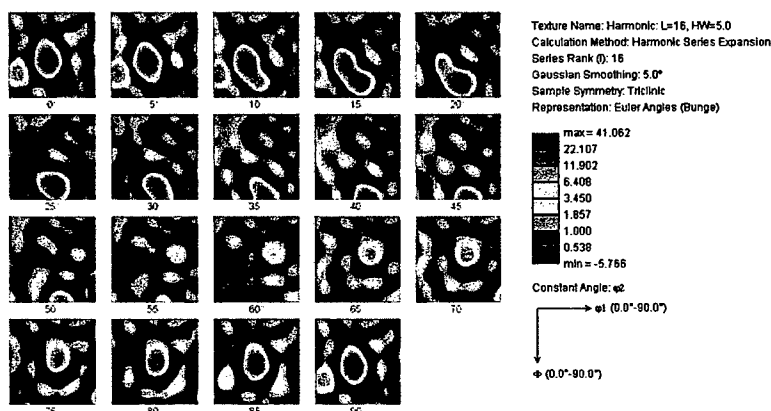
(c)

Fig. 26 (a) crack morphology and grain structure. (b) ODF of the recrystallized region ("A" in (a)), and (c) ODF of the unrecrystallized region ("B" in (a)) in the 2099 Al alloy.

4. Theoretical calculation

4.1 Mapping of the minimum twist angles

According to Zhai's crystallographic model for crack propagation through a grain boundary [6], the twist component of crack deflection across a grain boundary is the key factor controlling crack growth behavior. In order to understand the characteristic of the resistance of grain boundaries with different crystal geometry to crack growth, the possible smallest twist angle of crack plane deflection at the boundary between a grain with a special orientation (such as Brass or Goss) and a randomly orientated neighboring grain was calculated and mapped in Euler space [21]. Such a map represents how easy or difficult for a crack from the grain with a known orientation to propagate into the neighboring grain with any possible orientation. As shown in Fig. 27, this calculation includes the following steps: (1) Grain orientation selection of grains 1 and 2. Grain 1 is selected as the crack initiating site and assumed to have one of the commonly occurring orientations, e.g. Goss, brass, and cube orientations, etc. Grain 2 then has a random orientation, i.e., a single point in Euler space. (2) Crack slip plan determination. Since grains with large Schmid factors are the preferential site for short crack initiation, one of the {111} planes with the highest Schmid factor is chosen as the crack plane in grain 1. (3) Twist angle calculation. The details about calculation of the twist angle have been described in [6]. The twist angle of the crack plane in Grain 1 with each of the four {111} planes in Grain 2 is calculated. The smallest one is selected. (4) Mapping the smallest twist angle at the position of Grain 2 in Euler space. Varying the three Euler angles of Grain 2 in Euler space, the smallest twist angle is then calculated and plotted in Euler space. Such a process continues until all of Euler space is covered, as shown in Figs. 28 and 29. (5) Volume fraction calculation. The volume faction of twist angles within 5° in Euler space was quantified in each of these maps and used to evaluate the resistance of the special orientation to short crack propagation. A higher volume fraction means the worse resistance to short crack propagation.
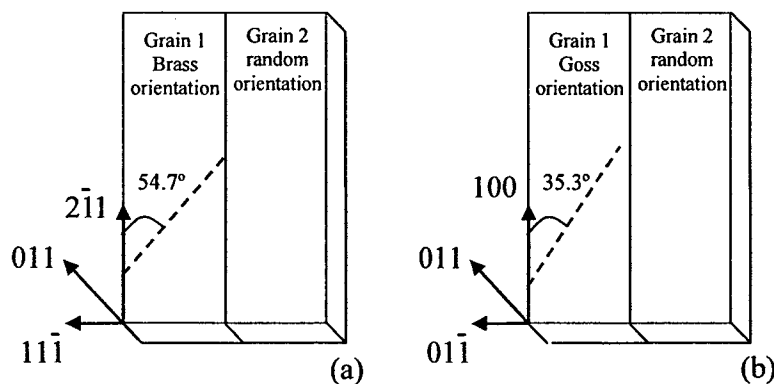

Fig. 27 Schematic diagrams showing orientations of two neighboring grains for calculation of the twist angle of crack plane deflection at their boundary. The grain 1 has a (a) Brass and (b) Goss orientation respectively. The dashed lines are the intercept lines of $(111)/(11\bar{1})$ plane (the crack plane) on the sample surface in grain 1.

As mentioned above, a crack is preferentially formed on a slip plane with the largest Schmid factor in these grains. In this study, one of the (111) planes, which has the largest Schmid factor, was selected as the crack plane when loaded in the rolling axis. The grain boundary plane was assumed to be parallel to the rolling axis and perpendicular to the sample surface. The intercept lines of this slip plane with the sample surface are shown as dashed lines in Fig. 27 in both the Brass and Goss grains. Grain 2 was given all the possible orientations by varying Euler angles, ϕ_1, Φ, ϕ_2, from 0° to 90° respectively. The twist angle of this crack/(111) plane in grain 1 with each of the four slip planes in grain 2 was calculated, and the minimum value was then selected as the possible twist component of crack plane deflection at the GB between grains 1 and 2.
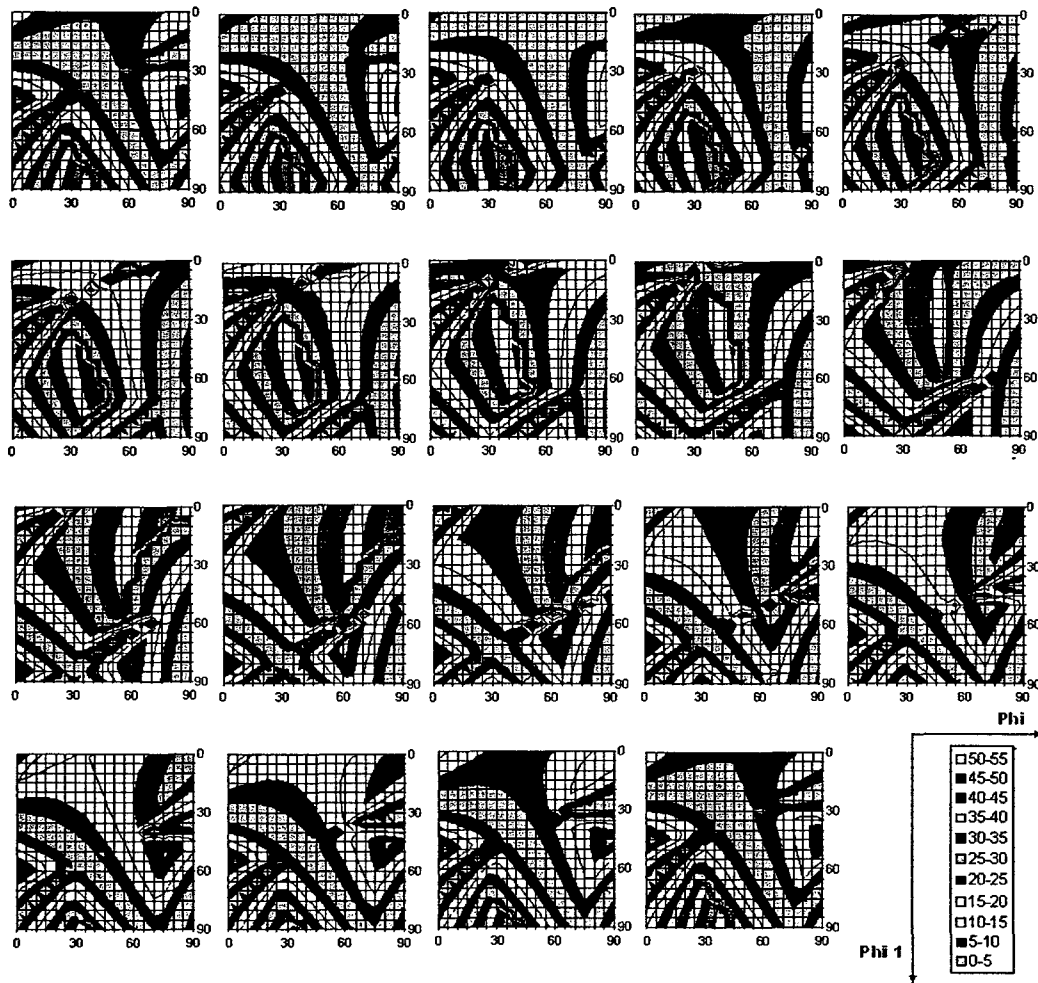

Fig. 28 Maps of the twist angle of crack deflection at the grain boundary between a Brass oriented grain and a randomly oriented grain in Euler space.
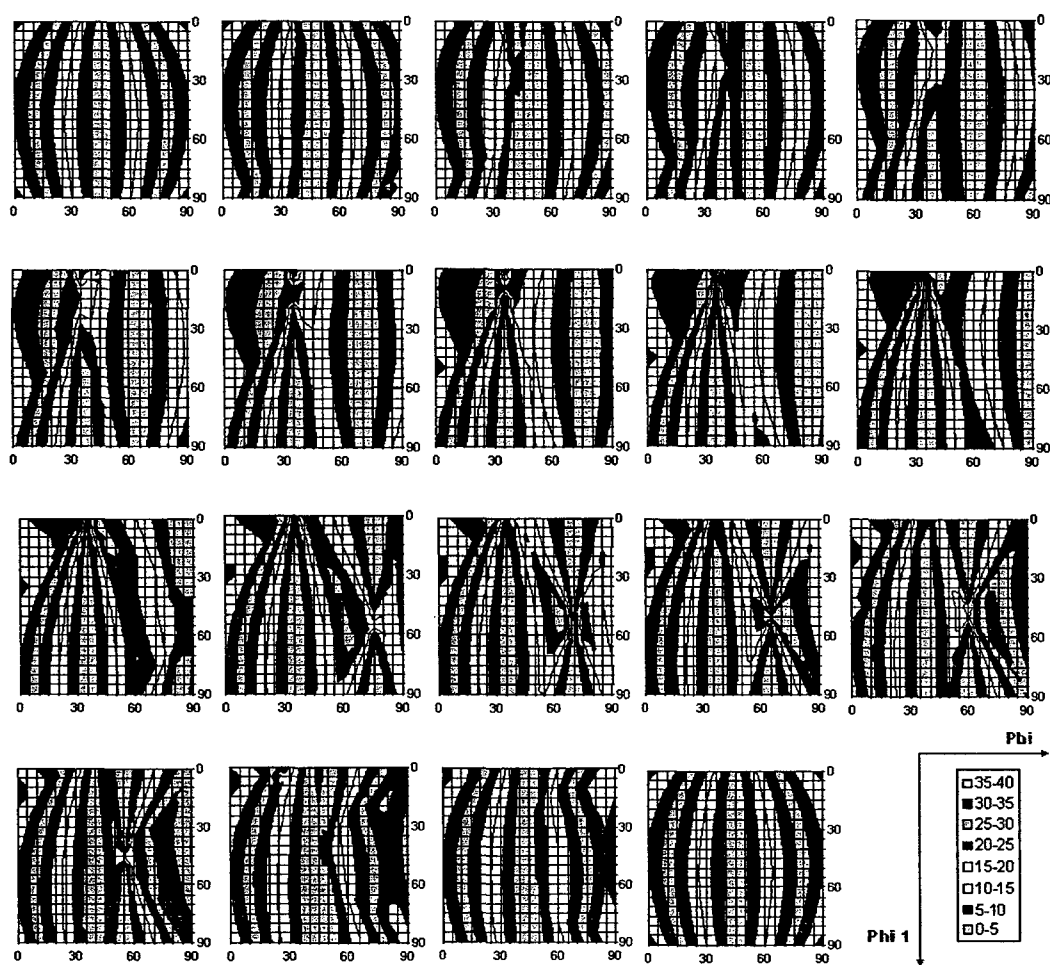
43

Fig. 29 Maps of the twist angle of crack deflection at the grain boundary between a Goss oriented grain and a randomly oriented grain in Euler space.

The calculated smallest twist angles were plotted in Euler space, as a series of $\phi_1 - \Phi$, sections each of which has a constant ϕ_2, as shown in Figs. 28 and 29. It can be seen that there is a much larger area where twist angles are within 5° in each $\phi_1 - \Phi$ section for the case of Brass orientation than Goss orientation. The total volume fraction of the region where the twist angle is within 5° in Euler space was calculated to be 20.3% and 16.9% for Brass and Goss orientations respectively. This indicates that it is much more likely for a crack in a Brass grain to propagate into its neighboring grain than in a Goss grain, in other words, Brass grains generally have less resistance to crack growth through their GBs than the Goss grains, though a crack my be more likely to be formed in Goss grains. Observation that the cracks formed in Goss grains mostly arrested at their boundaries provides the evidence supporting the result from the above twist angle calculations that Goss grains have higher resistance than brass grains to crack growth [22].

4.2 Short crack growth resistances of alloys with different texture components

The main purpose of this work was to establish a link between macro-texture and its resistance to crack growth, which could form a basis for optimum texture design of an alloy.

A computer program was written to compute the resistance to short crack growth, based on the macro-texture in an alloy. In this study, a simple layered grain structure was used, as that in AA2026 and 2099 Al alloys. Assume that there are 500 grains in the alloy. As shown in Table 6, based on the global texture measured using either XRD or EBSD in the alloy, these grains are assigned to each texture orientation by the number proportional to the volume fraction of the texture component. The two neighboring grains cannot have the identical orientation. After the assignment of orientation to all the grains, a micro-crack is assumed to take place in a grain with the largest Schmid factor and propagates. At each grain boundary that the crack interacts with, the minimum twist angle of crack plane deflection is calculated at each grain boundary along the crack path. The calculation process was repeated 5 times and the results were then averaged.
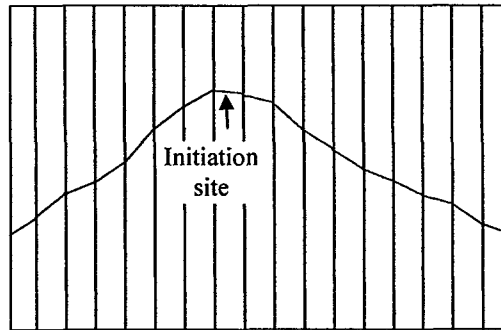

Fig. 30 Model grain structure for quantifying the resistance of an alloy, based on its global texture.

Two common types of textures were used in this calculation; one was typical rolling texture (Table 6) and the other ⟨111⟩ fiber texture. For the rolling texture, the twist angle distribution is shown in Fig. 31(a). A large percentage of twist angles of crack plane deflection was within 5°.

Table 6 Texture volume fraction and grain orientation distribution in a 2099 Al alloy

| Grain orientations	Euler angles	Percentage	Grains number (total: 500)
Brass {110}<112>	(35°, 45°,0°)	24%	120
S1 {124}<211>	(57°, 29°,63°)	18%	90
S3 {123}<634>	(59°, 37°,63°)	21%	105
Copper {112}<111>	(90°, 35°,45°)	15%	75
Taylor {4 4 11}<11 11 8>	(270°, 27°,45°)	19%	95
Cube {100}<001>	(0°, 0°,0°)	3%	15

In the case of a ⟨111⟩ fiber texture, as in square extrusion AA2026 and 2099 alloys, the orientation of each grain was defined by a rotation angle around the load axis, i.e., [111]

45

direction. The rotation was divided by a step of 5°. Since ⟨111⟩ directions have a 3-fold symmetry, the rotation angle was only taken from the range between 0° and 120°. There were 24 different rotation angles from 0° and 120°. 720 grains were taken into account, which means that every grain orientation was used 30 times. The 720 grains were then assigned randomly to a rotation angle from this range. If the rotation angles of two neighboring grains were within 15° in difference, the two grain were regarded as two subgrains in one grain, and, therefore, not allowed in this study.

The minimum twist angle between any two neighboring 111 fiber oriented grains was then calculated, as shown in Fig. 31(b). In comparison to the rolling texture, 111 fiber texture offered much less low angle twist grain boundaries. The grain boundaries with 0° to 5° twist angles were about 48% in the 111 fiber texture alloy, as compared to 65% in the rolling textured. This means that the 111 fiber textured alloy has resistance to fatigue crack propagation much higher than that in the rolling textured alloy, assuming that the resistance to the crack growth main results from the twist component of crack deflection across grain boundaries. This is consistent with the result that the 111 fiber textured AA2026 alloy shows a crack growth rate much lower than that in the rolling textured AA2026 alloy [8].
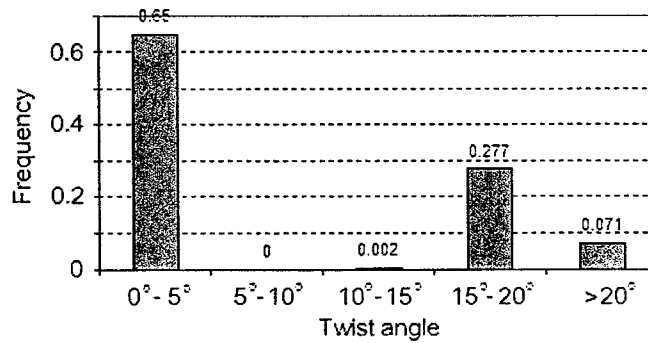
(a)
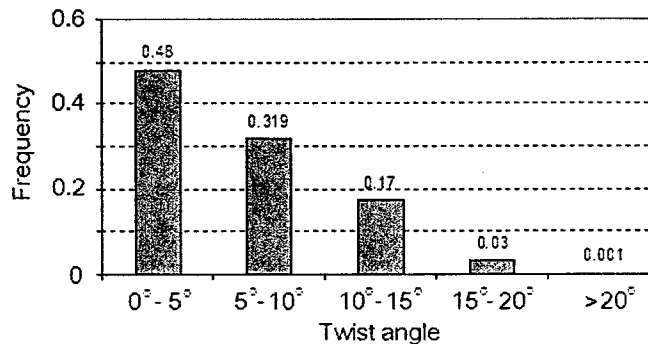
(b)

Fig. 31 Twist angle distribution of 2099 Al alloy with (a) grain orientations in table 6, and (b) 111 fiber texture.

Conclusions

- Short fatigue cracks were initiated in the α-phase grains of the Ti-6Al-4V alloy studied. They propagated crystallographically within the α-phase grains, and non-crystallographically in the β-phase grains. The fatigue life of the Ti-6Al-4V alloy was prolonged by shot peening or re-peening both at room temperature and at 150 °C.

- Commercially pure titanium specimens, which were sandblasted, exhibited higher HCF strength than the untreated titanium specimens. Annealing subsequent to sandblasting generated a nano-crystalline surface layer, which resulted in better corrosion performance of the specimens than sandblasting alone.

- After the surface enhancement treatments of shot peening and sandblasting, hardening textures were formed in the treated surface layer: a B-texture was formed in the Ti-6Al-4V alloy after shot peening and in pure titanium after sandblasting.

- The enhancement of fatigue properties by surface enhancement treatments was not only due to the formation of beneficial surface residual stress, but was also due to strain hardening, texture strengthening and grain refinement in the alloys studied.

- A method based on the macro-texture in an alloy was developed to evaluate the resistance to fatigue crack growth in the alloy.

- By studying the effects of micro- and macro-texture on fatigue properties in AA 2026 and 2099 Al alloys, it was found that, given the measured global texture and grain structure in these alloys, the resistance to crack growth could be quantified by calculating all the possible twist angles of crack deflection at grain boundaries,. This calculated resistance qualitatively correlated well with the observed crack growth behavior of these alloys.

- Further work needs to be done to quantify the growth behaviour of fatigue cracks in these alloys.

References

1. G.S. Was and R.M. Pelloux, *Met. Trans. A* 10 (1979) 656.

2. A. Drechsler, J. Kiese, and L. Wagner, *The 7th International Conference on Shot Peening*. Warsaw, Poland, 1999.

3. R.K. Nalla, I. Altenberger, U. Noster, G.Y. Liu, B.Scholtes, and R.O. Ritchie, *Mater. Sci. Eng. A* 335 (2003) 216.

4. P.S. Prevéy, J.T. Cammett, *Int. J. Fatigue* 26 (2004) 975.

5. S. Suresh, *Fatigue of Materials*, 2nd Edition, Cambridge University Press, Cambridge, UK 2001.

6. T. Zhai, A.J. Wilkinson, and J.W. Martin, *Acta Mater.* 48 (2000) 4917.

7. J.X. Li, T. Zhai, M.D. Garratt, and G.H. Bray, *Metall. Mater. Trans. A* 36 (2005) 2529.

8. M.D. Garratt, G.H. Bray, and D.A. Koss, *Proc: Materials Solutions Conference*, ASM International, Indianapolis, IN, 2001, pp. 151-159.

9. P.S. Precey, M.J. Shepard, and P.R. Smith, *Proceeding: 6th National Turbine Engine High Cycle Fatigue Conference*. Jacksonville, Florida, March, 2001.

10. Lambda Research. Effect of low plasticity burnishing on the HCF life of IN 718 alloy. *Diffraction notes*. 2000, 26.

11. R.S. Bellows, S. Muju, and T. Nicholas, *Int. J. of Fatigue* 21 (1999) 687.

12. S. Kodama, The behavior of residual stress during fatigue stress cycles. In: *Proceedings of the International Conference on Mechanical Behavior of Metals II*. Kyoto: Society of Material Science, 1972, 2:111-118.

13. W.J. Evans and C.R. Gostelow, *Met. Trans. A* 10 (1979) 1837.

14. R.K. Nalla, B.L. Boyce, J.P. Campbell, J.O. Peters, and R.O. Ritchie, *Metall. Mater. Trans. A* 33 (2002) 899.

15. T. Zhai, *Metall. Mater. Trans. A*, accepted.

16. Y.N. Wang and J.C. Huang, *Mater. Chem. Phy.* 81 (2003) 11.

17. L.B. Freund and S. Suresh, *Thin Film Materials: Stress, Defect Formation and Surface Evolution*, Cambridge University Press, Cambridge, 2003.

18. H.P. Klug and L. Alexander, *X-ray Diffraction Procedures for Polycrystalline and Amorphous Materials*, Wiley-Interscience, New York, 1974.

19. X.P. Jiang, X.Y. Huang, J.X. Li, D.Y. Li, C.-S. Man, M.J. Shepard, and T. Zhai, *Mater. Sci. Eng. A*, accepted.

20. X.Y. Wang and D.Y. Li, *Wear*, 255 (2003) 836.

21. T. Zhai, X.P. Jiang, J.X. Li, M.D. Garratt, and G.H. Bray, *Int. J. Fatigue* 27 (2005) 1202.

22. U.K. Kocks, C.N. Tomé, and H.-R. Wenk. *Texture and Anisotropy-Preferred Orientations in Polycrystals and Their Effect on Materials Properties*, Cambridge University Press, Cambridge, UK, 1998.